



HAL
open science

Cohesive properties of ice powders analogous to fresh plume deposits on Enceladus and Europa

Benoît Jabaud, Riccardo Artoni, Gabriel Tobie, Erwan Le Menn, Patrick Richard

► **To cite this version:**

Benoît Jabaud, Riccardo Artoni, Gabriel Tobie, Erwan Le Menn, Patrick Richard. Cohesive properties of ice powders analogous to fresh plume deposits on Enceladus and Europa. *Icarus*, 2024, 409, pp.115859. 10.1016/j.icarus.2023.115859 . hal-04290714

HAL Id: hal-04290714

<https://hal.science/hal-04290714>

Submitted on 17 Nov 2023

HAL is a multi-disciplinary open access archive for the deposit and dissemination of scientific research documents, whether they are published or not. The documents may come from teaching and research institutions in France or abroad, or from public or private research centers.

L'archive ouverte pluridisciplinaire **HAL**, est destinée au dépôt et à la diffusion de documents scientifiques de niveau recherche, publiés ou non, émanant des établissements d'enseignement et de recherche français ou étrangers, des laboratoires publics ou privés.

Highlights

Cohesive properties of ice powders analogous to fresh plume deposits on Enceladus and Europa

Benoît JABAUD, Riccardo ARTONI, Gabriel TOBIE, Erwan LE MENN, Patrick RICHARD

- Ice powders are characterised by a custom rotating drum at very low temperatures.
- Ice powder cohesion increases with the temperature over the range of 90 to 150 K.
- A mechanical model allows to estimate the grains surface energy from flow behaviour.
- Icy moons' regolith could see drastic cohesion change with diurnal cycles/location.

Cohesive properties of ice powders analogous to fresh plume deposits on Enceladus and Europa

Benoît JABAUD^{a,b}, Riccardo ARTONI^a, Gabriel TOBIE^b, Erwan LE MENN^b and Patrick RICHARD^a

^aMAST-GPEM, Université Gustave Eiffel, Allée des Ponts et Chaussées, Bouguenais, 44340, France

^bLaboratoire de Planétologie et Géosciences, UMR-6112, Nantes Université, 2 rue de la Houssinière, Nantes, 44322, France

ARTICLE INFO

Keywords:

Europa
Enceladus
Ices, mechanical properties
Regoliths

ABSTRACT

Active jets of water vapour and ice grains discovered by the *Cassini* spacecraft at the South Pole of Enceladus result in the deposit of freshly erupted materials on the icy surface of the moon, potentially coming directly from its subsurface water ocean. As suggested by sporadic detection of plume activity, similar processes may be at work on Europa as well. Such fresh ice deposit areas are primary targets for future landing and sampling missions for the search of potential bio-signatures. Determining the mechanical properties of such fresh icy powder-like materials is essential to identify safe landing sites and appropriate sampling techniques. Ice surface energy or cohesion is a key parameter driving the porosity of the material, its strength, stickiness and flowability, which determine the stability of fresh surface deposits. In this work we performed an experimental study on laboratory analogues of fresh icy regolith, consisting in investigating the flowability of ice powders through a rotating drum device at several temperatures. Our experimental results show that the flowability of fresh icy deposits significantly decreases with increasing temperatures over the range of 90 to 150 K. Using a simple scaling analysis, we derive the surface energy of ice grains from the observed angle of the flowing surface inside the drum and we show that the surface energy increase by a factor of 5 to 10 between 90 K to 150 K, a behaviour not observed in any other powder material. This result indicates that the flowability of fresh icy deposits at the surface of Enceladus and Europa should significantly change depending on the local surface temperature, which can vary spatially and temporally on the same range of temperature explored here. Due to lower gravity, ice powder will behave as a more cohesive powder on Enceladus than on Europa. Higher cohesion on Enceladus may result in the formation of a very loose regolith with high porosity, making stable landing more challenging. On Europa, the reduction of ice cohesiveness with decreasing temperature should help the flow of freshly eruptive granular ice materials, potentially explaining numerous flow features observed throughout the surface.

1. Introduction

In the outer solar system, and most particularly around the gas giants, most planetary objects display large amounts of solid water ice at their surface. The *Galileo* and *Cassini-Huygens* missions revealed that all the major icy moons of Jupiter and Saturn (i.e. Europa, Ganymede, Callisto, Enceladus and Titan) might possess a liquid water ocean beneath their icy shell (e.g. Nimmo and Pappalardo (2016)). In some cases, this ocean is modelled to be in direct contact with the rocky core of the body (Sotin and Tobie, 2004; Kuskov and Kronrod, 2005; Schubert, Anderson, Travis and Palguta, 2007; Schubert, Sohl and Hussmann, 2009; Iess, Stevenson, Parisi, Hemingway, Jacobson, Lunine, Nimmo, Armstrong, Asmar, Ducci and Tortora, 2014), possibly leading to hydro-thermal processes similar to those observed on Earth's seafloor (Lowell and DuBose, 2005; Vance, Harnmeijer, Kimura, Hussmann, deMartin and Brown, 2007; Glass, Dierssen, Glein, Schmidt and Winebrenner, 2022). These hydrothermal vents may provide energy and elements that can be useful for the emergence and the development of life (Shock, 2007; Martin, Baross, Kelley and Russell, 2008; Hand, Sotin, Hayes and Coustenis, 2020). Saturn's moon Enceladus and Jupiter's moon Europa are the two best candidates where such hydrothermal activities are expected, making them primary targets for the search of environments suitable for extraterrestrial life (Hand et al., 2020; Choblet, Tobie, Buch, Čadek, Barge, Běhounková, Camprubi, Freissinet, Hedman, Jones, Lainey, Le Gall, Lucchetti, MacKenzie, Mitri, Neveu, Nimmo, Olsson-Francis,

*Corresponding author

✉ benoit.jabaud@univ-eiffel.fr (B. JABAUD)

ORCID(s): 0009-0000-9513-9221 (B. JABAUD)

Panning, Postberg, Saur, Schmidt, Sekine, Shibuya, Sotin, Soucek, Szopa, Usui, Vance and Van Hoolst, 2021). Owing to their very active surfaces revealing on-going exchanges with the subsurface ocean, among the different ocean world candidates, Enceladus and Europa are the two moons where the chances to find bio-signatures at their surface are the highest, especially in freshly deposited areas.

Despite its small size (only 504 km in diameter), Enceladus is the only icy body for which direct observations of water ice eruptions have been made. Its surface is the brightest of the solar system, covered by very young (less than a few million years old, down to < 500, 000 years old) water ice at the South Pole (Porco, Helfenstein, Thomas, Ingersoll, Wisdom, West, Neukum, Denk, Wagner, Roatsch, Kieffer, Turtle, McEwen, Johnson, Rathbun, Veverka, Wilson, Perry, Spitale, Brahic, Burns, DelGenio, Dones, Murray and Squyres, 2006; Robidel, Le Mouélic, Tobie, Massé, Seignovert, Sotin and Rodriguez, 2020). Thanks to the *Cassini-Huygens* mission, jets of water vapour and microscopic ice grains have been discovered (Porco et al., 2006; Waite, Combi, Ip, Cravens, McNutt, Kasprzak, Yelle, Luhmann, Niemann, Gell, Magee, Fletcher, Lunine and Tseng, 2006; Hansen, Esposito, Stewart, Colwell, Hendrix, Pryor, Shemansky and West, 2006; Spahn, Schmidt, Albers, Hörning, Makuch, Seiß, Kempf, Srama, Dikarev, Helfert, Moragas-Klostermeyer, Krivov, Sremčević, Tuzzolino, Economou and Grün, 2006), forming a plume emerging from > 100 km long thermally active fractures at the south pole, called Tiger Stripes (Porco et al., 2006; Spencer, Pearl, Segura, Flasar, Mamoutkine, Romani, Buratti, Hendrix, Spilker and Lopes, 2006). The jets particles are mostly composed of water ice, but a small fraction displays 0.1 – 0.4 % of salt and up to 0.01 – 0.3 % of organic compounds (Postberg, Schmidt, Hillier, Kempf and Srama, 2011; Postberg, Khawaja, Abel, Choblet, Glein, Gudipati, Henderson, Hsu, Kempf, Klenner, Moragas-Klostermeyer, Magee, Nölle, Perry, Reviol, Schmidt, Srama, Stolz, Tobie, Trieloff and Waite, 2018b; Postberg, Clark, Hansen, Coates, Dalle Ore, Scipioni, Hedman and Waite, 2018a). Due to the size of the moon, most of the particles can escape Enceladus' gravity to feed the E ring of Saturn (Spahn et al., 2006; Kempf, Beckmann and Schmidt, 2010), but the grains larger than a ~ 5 µm fall back at the surface of the moon with a defined pattern (Schmidt, Brilliantov, Spahn and Kempf, 2008; Schenk, Hamilton, Johnson, McKinnon, Paranicas, Schmidt and Showalter, 2011), creating a global ice powder layer, estimated to be locally as thick as 700 m (Martin, Whitten, Kattenhorn, Collins, Southworth, Wiser and Prindle, 2023), that can carry potential bio-signatures coming from the deep ocean. The largest grains falling back near the jet sources (Jaumann, Stephan, Hansen, Clark, Buratti, Brown, Baines, Newman, Bellucci, Filacchione et al., 2008; Taffin, Grasset, Le Menn, Bollengier, Giraud and Le Mouélic, 2012), the likelihood of collecting materials with detectable amounts of bio-materials is highest at the vicinity of the Tiger Stripes.

Like Enceladus, Jupiter's moon Europa is expected to possess liquid bodies at depths of 30 km maximum, allowing eruptions of fresh materials (Fagents, 2003; Schmidt, Blankenship, Patterson and Schenk, 2011; Lesage, Massol and Schmidt, 2020; Quick and Hedman, 2020). Several darkish/brownish features identified at the surface, associated either to tectonic activity or chaotic terrains (Fagents, Lopes, Quick and Gregg, 2022), suggest relatively recent eruptions, although precise age cannot be estimated. Some observations support the presence of a possible water plume emitted in a process similar to Enceladus (Roth, Saur, Retherford, Strobel, Feldman, McGrath and Nimmo, 2014; Sparks, Hand, McGrath, Bergeron, Cracraft and Deustua, 2016; Sparks, Schmidt, McGrath, Hand, Spencer, Cracraft and Deustua, 2017), suggesting on-going but sporadic eruption activities. The ESA *JUICE* mission launched in April 14, 2023 (Grasset, Dougherty, Coustenis, Bunce, Erd, Titov, Blanc, Coates, Drossart, Fletcher, Hussmann, Jaumann, Krupp, Lebreton, Prieto-Ballesteros, Tortora, Tosi and Van Hoolst, 2013), and the NASA *Europa Clipper* mission (Howell and Pappalardo, 2020), planned for launch in Oct. 2024, will be able to detect and analyse those potential plumes. Considering the estimated surface age of Europa - 40 to 90 Myr (Zahnle, Schenk, Levison and Dones, 2003; Bierhaus, Zahnle and Chapman, 2009) - it is plausible that a process of constant deposition of fresh material is taking place on Europa, although the eruption process should be somewhat different from Enceladus due to differences in gravity and tidal forcing.

The measurements performed by *Cassini* on Enceladus provided some constraints on the characteristics of ice particles ejected from the south pole faults. Using the infrared channel of the Visual and Infrared Mapping Spectrometer (VIMS) instrument to observe Enceladus' plume, Hedman, Nicholson, Showalter, Brown, Buratti and Clark (2009) determined that the particles of the plume were composed of small grains (< 5 µm), while Hillier, Green, McBride, Schwanethal, Postberg, Srama, Kempf, Moragas-Klostermeyer, McDonnell and Grun (2007) determined that the grain population of the E ring was composed of 99 % of water ice particles. Spectra acquired at different altitudes in the plume also showed some variations in the spectral response of the material, translated into velocity distribution of the particles, leading to more constraints for models of particles launch and deposition. The VIMS instrument also provided constraints on the spatial distribution of the ice grain average size at the surface of Enceladus, indicating a spatial sorting of the particles with distance to the Tiger Stripes features (Jaumann et al., 2008; Taffin et al., 2012).

The bigger grains are found close to the stripes, according to the VIMS data that shows a peak in the distribution around 40 μm . Further from the stripes, the particle distribution suggests a peak around 20 μm . These results imply that the smaller grains can travel further from the ejection source, and probably leave the gravitational influence of Enceladus for the smallest ones. The Cosmic Dust Analyser (CDA, Srama, Ahrens, Altobelli, Auer, Bradley, Burton, Dikarev, Economou, Fechtig, Görlich, Grande, Graps, Grün, Havnes, Helfert, Horanyi, Igenbergs, Jessberger, Johnson, Kempf, Krivov, Krüger, Mocker-Ahltreep, Moragas-Klostermeyer, Lamy, Landgraf, Linkert, Linkert, Lura, McDonnell, Möhlmann, Morfill, Müller, Roy, Schäfer, Schlotzhauer, Schwehm, Spahn, Stübig, Svestka, Tschernjawski, Tuzzolino, Wäsch and Zook (2004)), an instrument designed to sample grains when the spacecraft is flying at high velocity through a particle formation like the rings of Saturn or the plumes of Enceladus, confirms this behaviour. By sampling icy grains at high velocity, this instrument allowed to determine that Saturn's E ring was composed from the smallest grains ejected from the surface of Enceladus ($\sim 0.1\text{-}10 \mu\text{m}$, Kempf, Beckmann, Moragas-Klostermeyer, Postberg, Srama, Economou, Schmidt, Spahn and Grün (2008)).

From the information extracted from these instruments, models of material ejection have been proposed to determine the particle flux emanating from Enceladus' plume. Schmidt et al. (2008), from a model of a vent going through Enceladus's ice surface, explained the velocity difference observed between the ice grains and the water vapour inside the plume. Their results indicate the presence of a liquid source beneath the surface and they estimate a particle mass flux of $\sim 5 \text{ kg}\cdot\text{s}^{-1}$, with only 10 % of this flux escaping Enceladus, and a grain size distribution around the micrometer range. Nakajima and Ingersoll (2016) and Ingersoll and Nakajima (2016), following the same idea, developed models of vapour and ice grain dynamics through cracks to explain the characteristics of the observed plumes. They explained the estimated mass flux by ideal crack widths of 0.05-0.75 m, with narrower and deeper cracks producing a more important mass flux. Their model also argues in favour of a liquid source beneath the surface, potentially connected to the subsurface ocean, boiling into space to create the plume, and they also argue that a salinity of at least $\sim 20 \text{ g}\cdot\text{kg}^{-1}$ is required to prevent freezing of the boiling surface. Kempf et al. (2010) used numerical simulations of grain ejections to reproduce the vertical structure of the E ring observed by the CDA instrument. From these simulations, they have been able to calculate the deposition rate at the surface of Enceladus, deducing that at 100 m from the ejection point, only $10^5\text{-}10^6$ years are required to cover a 10 m boulder.

From the localisation of the jet sources, estimated by Spitale and coworkers (Spitale and Porco, 2007; Porco, DiNino and Nimmo, 2014; Spitale, Hurford, Rhoden, Berkson and Platts, 2015), deposition maps for grains ranging from 0.6 to 15 μm have been estimated by Southworth, Kempf and Spitale (2019). These maps show very clearly the wider spatial extent of the smaller grains at the surface of Enceladus, previously mentioned. All the analyses tend to show that the typical grain sizes found on Enceladus are ranging from a few micrometres (far from Tiger Stripes) to a few tens of micrometres near the ejection point.

On Europa, spectral data provided by the Near-Infrared Mapping Spectrometer instrument (NIMS) onboard the *Galileo* mission were analysed using reflectance models that indicate radii ranging between 20 and 50 micrometres (Hansen and McCord, 2004). However, this size estimation is not as well constrained as on Enceladus, as there is no direct observation of a plume activity at Europa, and no sampling of the grains. Remotely, data acquired with the *Hubble Space Telescope* (HST) indicates the presence of a plume activity on Europa, through the detection of water vapour above the southern hemisphere. Roth et al. (2014) used UV-observations made by the HST to infer the potential existence of two 200 km high plumes of water vapour at the surface of Europa, with a sporadic activity. Sparks et al. (2016) used HST direct observations of Europa's transit in front of Jupiter to corroborate this idea, and detected features consistent with Roth et al. (2014) observations and close to the crater Pwyll. Fifteen years after the end of the *Galileo* mission, Jia, Kivelson, Khurana and Kurth (2018) revisited magnetic and plasma wave signatures acquired during the closest flyby to Europa. They discovered large scale magnetic field rotation and a significant decrease in the magnetic field magnitude, together with an increase of the plasma density near Europa's surface. These results are consistent with the presence of a plume with the characteristics inferred from HST images, interacting with Jupiter's plasma. Southworth, Kempf and Schmidt (2015), based on the results obtained for Enceladus, developed a model of Europa's potential plume. They deduced some information about the extent of the plume feature, making it detectable only at low altitude, and also first insights of grain deposition patterns at the surface of Europa, considering small ice grains of $\sim 0.6\text{-}5 \mu\text{m}$, similar to the typical size of ejected grains on Enceladus.

Considering the nature of the particle ejection process on Enceladus and potentially on Europa, the fresh deposits should consist in a very fine granular material behaving as powder. This peculiar type of material, because of the properties of the ice itself and the very small grains, is subject to potentially very high cohesion forces that could have key implications for the morphological identification of fresh deposits and potential future samplings.

Cohesion can greatly influence the flow stability of surface deposits and can thus control their morphology, and determine the apparent porosity and strength of superficial powdered layer, challenging future landing. This parameter is also controlling the flowability and stickiness of the ice powders, essential properties to determine in order to develop optimal sampling methods to be used by future landers (Badescu, Riccobono, Ubellacker, Backes, Dotson, Molaro, Moreland, Csomay-Shanklin, Choukroun, Brinkman and Genta, 2019; Hand, Phillips, Murray, Garvin, Maize, Gibbs, Reeves, Martin, Tan-Wang, Krajewski, Hurst, Crum, Kennedy, McElrath, Gallon and 272 authors, 2022). The characterisation of the mechanical properties of planetary surfaces, such as their cohesion, is key to avoid technical issues, as it has been unfortunately illustrated by the *InSight* mission with the HP3 instrument. This instrument was designed to drill in the martian regolith up to 5 m to measure the heat flux, but due to poor constraints on the properties of the martian regolith at this location, the head of the instrument was only able to penetrate the regolith for a few tens of centimetres. On a more positive note, the *Philae* lander from the *Rosetta* mission, despite the failure of its landing system and multiple rebounds at the surface of the comet 67P/Churyumov-Gerasimenko, revealed an unexpected behaviour of the material at the impact points (O'Rourke, Heinisch, Blum, Fornasier, Filacchione, Van Hoang, Ciarniello, Raponi, Gundlach, Blasco, Grieger, Glassmeier, Küppers, Rotundi, Groussin, Bockelée-Morvan, Auster, Oklay, Paar, del Pilar Caballo Perucha, Kovacs, Jorda, Vincent, Capaccioni, Biver, Parker, Tubiana and Sierks, 2020). The excavated material analysed with the *Rosetta* spacecraft showed a composition rich in water ice, and a very low compressive strength of less than 12 Pa, leading to an estimation of the porosity of this material of $75 \pm 7\%$ (O'Rourke et al., 2020). This result shows the importance of the cohesion for planetary surfaces, which can create very loose structures of low density that need to be anticipated for future landing missions.

While the nature of icy regolith may vary depending on the icy surface target, here we focus, as a first approach, on pure water ice powders, which are likely good analogues of freshly erupted ice deposits on Enceladus, and could constitute a first attempt to study similar deposits on Europa. Pure water ice powders were also used in most studies (Gundlach, Kiliyas, Beitz and Blum, 2011; Gundlach and Blum, 2015; Musiolik and Wurm, 2019; Choukroun, Molaro, Hodyss, Marteau, Backes, Carey, Dhaouadi, Moreland and Schulson, 2020), but this has not to be seen as a limitation, because controlled laboratory analogues and experiments provide clues on the effect of physical parameters, such as grain size or temperature, on the mechanical properties of such materials. All these studies on pure ice powders may therefore help in constraining the estimations of the properties of real regoliths and, as discussed above, little is known on the physical properties of such deposits on Enceladus and Europa, at the exception of a rough estimate of grain size. Previous works have already been done on icy regolith analogues, at different scales, to try to determine the mechanical properties of ice powders. On a macroscopic scale, Choukroun et al. (2020) conducted several penetrometer experiments on fine ice powders to determine the evolution of the strength of the material as a function of the time and temperature and investigate the effect of sintering processes relevant for temperatures above 193 K. At the grain scale, Gundlach et al. (2011) studied the surface energy and the rolling friction of micrometer-sized ice particles at relatively high temperatures (189-226 K). The surface energy is a variable quantifying the strength of interparticle adhesion. It represents the energy required to create a surface unit at the contact between two grains, and is expressed in $\text{J}\cdot\text{m}^{-2}$. It is therefore a measure of the interparticle adhesion, and can be estimated by using different experimental techniques, notably rotating drum experiments as we show hereafter. Cohesion is on the other hand a more generic word, which can be used both for addressing the macroscopic non-free flowing behaviour of a fine powder, but also the adhesion at the particle scale. Gundlach and Blum (2015) investigated the growth and erosion of ice grain aggregates between 114 K and 260 K in the context of ice accretion in planetary disks. At the particle scale, Musiolik and Wurm (2019) investigated the contacts of water ice grains in the context of proto-planetary disks through sticking force measurements, to determine the evolution of the cohesion of ice grains with respect to the temperature, at relatively high temperature (175-233 K). These results suggest a link between the cohesion of ice and its temperature, but the temperature range is much higher than the surface conditions on icy moons (< 130 K).

While all the techniques presented here aim at characterising the surface energy of ice powders, they involve different experimental setups. It is important to keep in mind that they are often based on the quantification of the macroscopic effect of the particle-scale adhesion, and therefore consist in indirect estimations of the surface energy, by means of a mathematical model of the phenomenon. It is then difficult to directly compare them between each other, but the order of magnitude of the surface energy should remain close, which is the case in all the previously mentioned studies. If the techniques are not directly comparable, they are more useful in a relative characterisation, meaning that they can study the influence of many physical parameters (such as grain size, grain shape, temperature...) on the estimation of the surface energy.

In this work we develop a macroscopic test in order to characterise the effective cohesion of unconsolidated ice powders *via* the measurement of the dynamic angle of repose in cryogenic conditions. The setup allows us in particular to highlight the effect of temperature and particle size on this dynamic angle of repose, using a rotating drum device cooled with liquid nitrogen to achieve temperatures as low as 90 K. From image analysis of the flowing material inside such a drum, we can extract the dynamic angle of repose and its variations, and link this parameter to the surface energy of the studied material. In Sec. 2 we present the methods used in this work to produce icy fresh deposit analogues and characterise their grain size distribution, as well as the experimental drum device. Then we present the results obtained on reference and ice powders with this device in Sec. 3. Finally, Sec. 4 will present a discussion around these results, to estimate the surface energy of ice grains through an avalanche model, and to explore the implications of such estimations for the surface state of Enceladus and Europa.

2. Methods

2.1. Icy regolith analogues synthesis

One of the hypotheses considering the formation of icy grains in the jets observed on Enceladus by *Cassini* consists of vapour bubbles bursting at the surface of water filling the icy cracks in Enceladus' shell, projecting through the vents very small droplets of liquid water and vapour (Postberg et al., 2018b). Due to the very low temperature in the vent conduits, the tiny water droplets freeze to produce ice grains likely spherical. Sampling by the Cassini spacecraft (Spahn et al., 2006), remote observations (Hedman et al., 2009; Porco et al., 2006) as well as eruption models (Schmidt et al., 2008; Ingersoll and Nakajima, 2016) also indicate a typical grain size around a few micrometers for the fastest grains ejected at very high altitudes, and typically tens to hundred of micrometers for the slowest grains deposited in the vicinity of the jet sources (Jaumann et al., 2008; Taffin et al., 2012).

As an analogy to these jets processes on Enceladus, one of the most common ways to produce ice powders mimicking possible fresh surface deposits on icy moons is to inject very small water droplets into a liquid nitrogen bath at -195.79°C (Gundlach et al., 2011; Yoldi, Pommerol, Jost, Poch, Gouman and Thomas, 2015; Jost, Pommerol, Poch, Gundlach, Leboeuf, Dadras, Blum and Thomas, 2016; Poch, Pommerol, Jost, Carrasco, Szopa and Thomas, 2016; Poch, Cerubini, Pommerol, Jost and Thomas, 2018; Choukroun et al., 2020; Stephan, Ciarniello, Poch, Schmitt, Haack and Raponi, 2021). This allows the droplets to freeze in a few seconds at cooling rates allowing the ice to be crystalline (water droplets may not freeze instantly due to Leidenfrost effect, see Cerubini, Pommerol, Yoldi and Thomas (2022), but may freeze on very short timescales, depending on particle size), producing spherical ice grains which size is determined by the pressurised device used to produce the droplets. We use this principle to produce grains of interest for our study.

We use an industrial nozzle, usually made for coating, the AN9010SS from the EXAIR company. This device works with pressurised liquid coming by one side, and pressurised gas coming by the other side. Liquid and gas mix inside the nozzle, allowing the gas to shear the liquid flow and to break it into very small droplets that are then ejected by the pressure inside the nozzle. The droplets' fog then created is shaped by the outlet to produce a cone jet with a narrow angle. By controlling the liquid and gas pressure separately, it is possible to change the size of the produced droplets.

For our application, we use ultra-pure water as the liquid, and dry pressurised air as the driving gas. The water fog then produced is injected into a Dewar filled with liquid nitrogen to freeze the droplets. A sketch of the ice grains production device is presented in Fig. 1. Due to the pressure of the jet, a large fraction of the water droplets are pushed against the walls of the Dewar, where they condense to form a frost deposit considered as a contaminant in our case. To get rid of this deposit, we place inside the Dewar a pipe that has almost the same diameter, and that goes all the way up to the opening, above the liquid nitrogen level to collect all the frost. Doing this allows us to remove the frost deposits by removing the pipe at any moment.

With this production device, we are able to produce the quantity of ice powder (with controlled grain size) needed for one drum experiment (around 20 g) in around fifteen minutes. Once we produced the ice particles, we let the nitrogen evaporate almost entirely, and we sieve the remaining mixture of liquid nitrogen and ice particles to prevent any possible contamination by large aggregates. We then transfer this final refined powder sample into a plastic container with liquid nitrogen, and store it in a Dewar full of nitrogen to keep the sample at very low temperature.

With the method described above, we are able to produce two ice powder populations with spherical shapes (Fig. 2), but with different grain size distributions, by changing both the air and liquid pressure in agreement with the technical

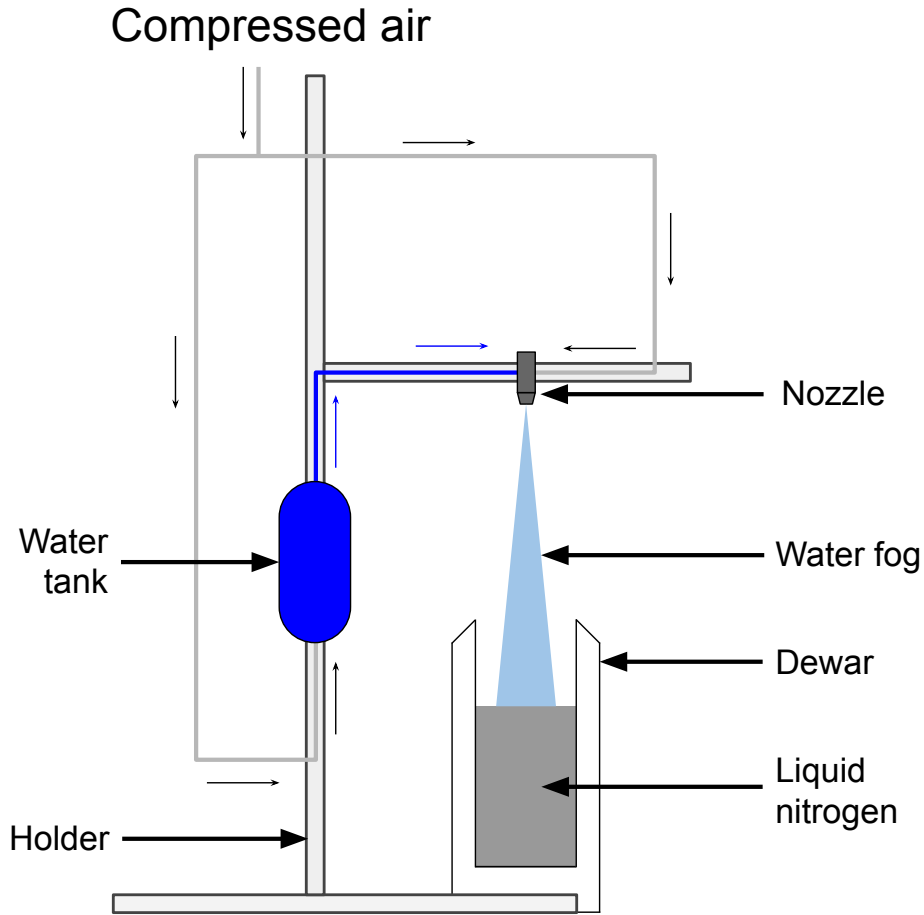


Figure 1: Scheme of the ice grains production device.

specifications of the nozzle (only some combinations of pressure are able to produce droplets). The size distributions for these two ice powders are given in Sec. 2.2.

For sake of comparison, we are also using non-ice powders in our characterisation methods, with different cohesion properties. On one hand, we use a glass beads powder with a median diameter of $36\ \mu\text{m}$. This powder behaves as weakly cohesive. On the other hand we are using a calcareous powder (Betocarb HP-EB, composed at 97.3% of CaCO_3) referred to as limestone powder in the following, with angular and very small grains (median diameter of $17\ \mu\text{m}$). By visual inspection only and the way this powder behaves when handled, we consider this powder as highly cohesive.

2.2. Optical Characterisation

Given that the effective cohesion of a powder depends on particle size, one of the most important parameters to know for our powders is the grain size distribution. For the limestone powder and the glass beads, the particle size distribution was measured with a laser diffraction granulometer (Fritsch Analysette 22). For ice powders, due to the constraints of the material (low temperature, fine particle size) it was not possible to use standard techniques such as sieving or laser diffraction to determine the particle size distribution, but an ad-hoc procedure by means of a digital microscope was adopted instead.

We used the digital microscope KEYENCE VHX-2000. This device allows us to take pictures and measure the dimensions of the grains, at a magnification between $\times 200$ and $\times 400$. It is coupled with a cryostat device, in order to keep our grains in a controlled atmosphere in terms of temperature and pressure. With a liquid nitrogen

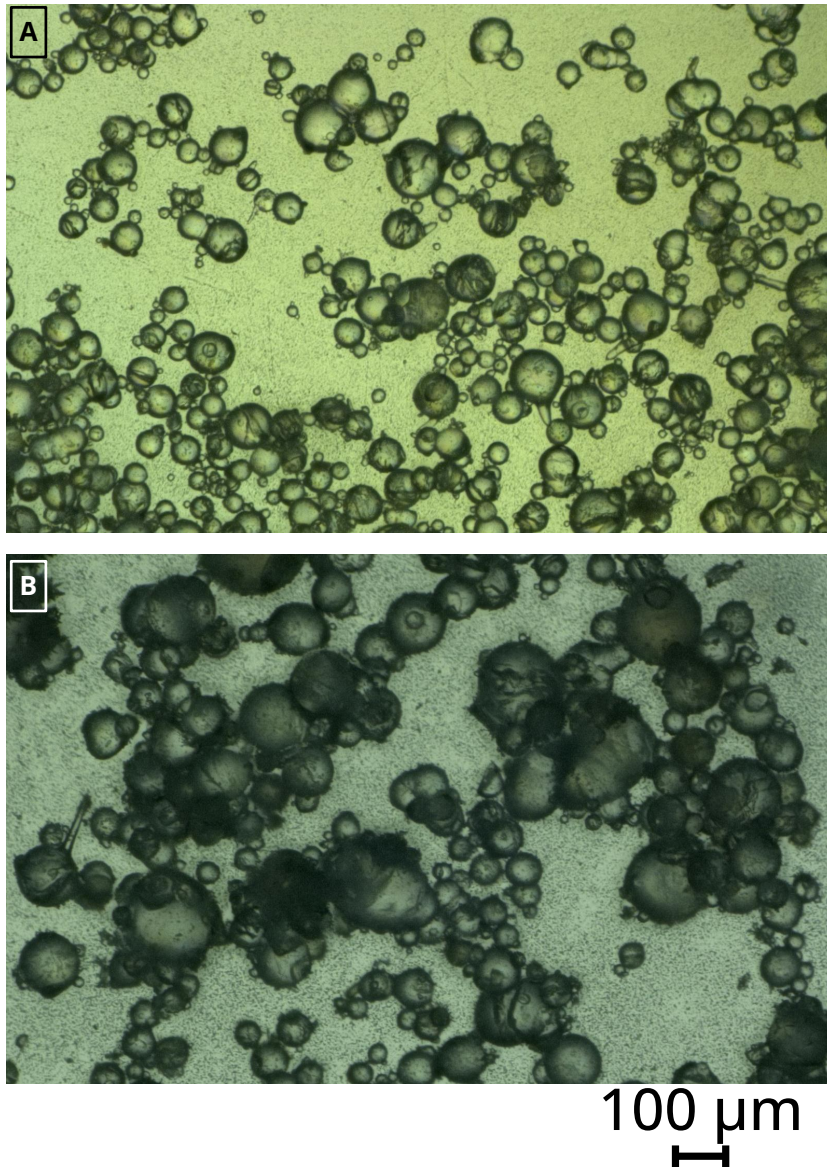


Figure 2: Examples of images of our ice powder samples. Powder A and B are indicated by their corresponding letters on the figure.

circulation around a copper sample holder, the temperature inside the cryostat goes down to ~ 90 K, preventing sublimation/condensation and sintering processes of the ice during the whole duration of the observation. The cryostat is sealed, and a vacuum pump allows us to lower the pressure down to $\sim 10^{-1}$ mbar, thus preventing the contamination of the sample by atmospheric water vapour. Two sapphire windows at the bottom and on the lid of the cryostat, and one at the bottom of the sample holder, allow clear observations of the sample with the optical microscope.

To measure the size of the grains in our samples, we need a relatively large amount of measurements. For each sample, we take four to five images of the grains, with a depth composition processing technique. This technique allows us to take images at different focus levels, to combine them in a single fully-focused image of our grains. With this technique, small and big grains appear focused even in different focal planes, and it is easier to measure all the grain populations in a single image (Fig. 2). Once an image is acquired, we then use the measurement techniques proposed

Cohesive properties of ice powders

Powder	Density(kg/m ³)	d20(μm)	d50(μm)	d80(μm)
Limestone	2700	4.0	17.1	66.7
Glass Beads	2600	23.2	36.1	50.0
Ice Powder A	940	56.7	84.0	117.2
Ice Powder B	940	90.6	134.4	192.8

Table 1

Particle density and size distributions for all the model samples and the ice samples.

by the microscope software: for grains produced by spraying, we use a circle approximation to measure the diameter of the grains.

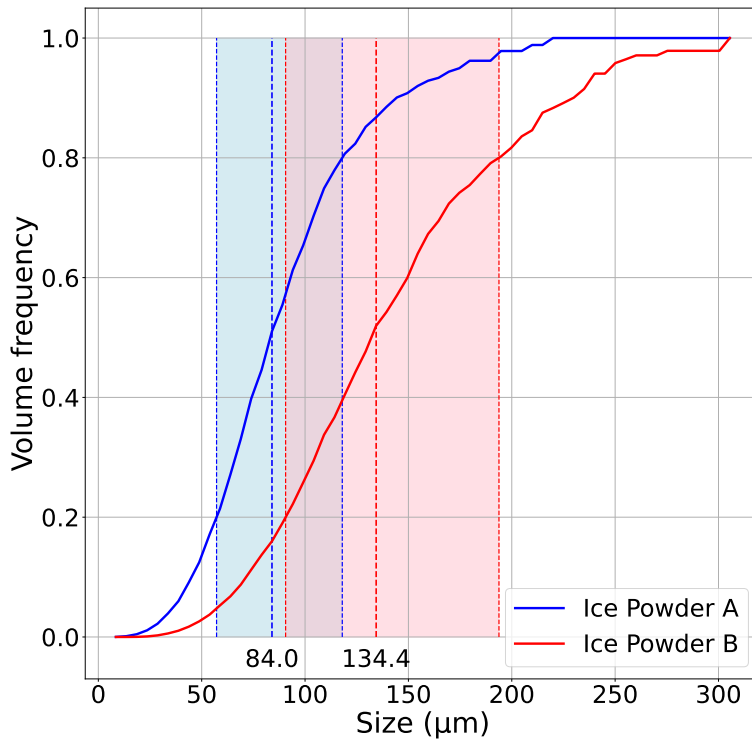


Figure 3: Cumulative frequency for the two ice powder samples, in terms of volumes of the grains.

The grain size distributions obtained with the digital microscope device and protocols for ice powders are presented in Fig. 3. A summary of some properties of all the interesting powders of this study is presented in Table 1. It is important to notice here that the median volumetric sizes of our two ice powder samples are slightly higher than the ones estimated on Enceladus and Europa, but remain comparable to the estimate based on infrared spectra, especially along the Tiger Stripes on Enceladus (Taffin et al., 2012; Spencer and Nimmo, 2013). However, this campaign is focused on the effect of temperature and grain size on the mechanical properties of ice powders, as an analogue of icy regoliths, that are mostly composed of water ice. An exact reproduction of this regolith is therefore not required here.

2.3. Rotating Drum Device

2.3.1. Working principles

The rotating drum device is an experimental tool that allows the measurement of the dynamical behaviour of a powder in rotation inside an horizontal cylindrical drum, to access some interesting parameters such as the dynamic angle of repose with continuous flows, the avalanche triggering angles, maximum and minimum angle of repose before and after an avalanche for discontinuous motions at low rotation speed. For non-cohesive materials, many flowing regimes have been described as a function of the filling ratio of the drum and the rotation speed, represented by a dimensionless number called the Froude number (Mellmann, 2001). This number describes the relative importance of the centrifugal force with respect to gravity, following this formula:

$$Fr = \frac{\omega^2 R}{g}, \quad (1)$$

where ω represents the rotation speed of the drum, in $rad.s^{-1}$, R is the radius of the drum in m , g is the gravity, in $m.s^{-2}$. Different devices operating at the same Froude number should experience the same powder behaviours, allowing to scale the input parameters of the experiment, such as the rotation speed, with the size of the device.

According to Mellmann (2001), for cohesion-less materials it is possible to identify different flowing regimes inside a rotating drum, depending on the rotation speed, from slipping as a block against the wall to the centrifugation of the material. However, these regimes are not all present for cohesive powders. Such powders tend to form strong aggregates, thus inhibiting the continuous flows usually observed to produce irregular avalanches for the whole range of rotation speeds. Therefore, the cohesive properties of the grains will allow higher values of surface angles before creating an avalanche, and the surface of the powder will display a lot more irregularities for cohesive powders. Characterising the angle of the flowing surface of a powder and its variations inside a drum then allows to quantify the cohesion of different powders (Lumay, Boschini, Traina, Bontempi, Remy, Cloots and Vandewalle, 2012). In this study, we performed measurements at different rotation speeds, to check if this parameter still has an effect on the behaviour of the powder, and to check the robustness of the results with respect to this parameter.

2.3.2. Cold temperature experiment

The purpose of the rotating drum is to characterise the cohesion of different ice powders, and to evaluate the eventual influence of the temperature on this parameter. While rotating drums are routinely used for various applications in industry and in granular physics research, no device operating at very low temperature exists. For that purpose, we developed a rotating drum device inspired by Lumay et al. (2012), but adapted to very cold temperature conditions to work with ice powders and to get as close as possible to the temperature conditions at the surface of icy moons. A complete description of the experimental device we developed for this study is available in Supplementary Online Material. We built an all-brass drum with a diameter of 64 mm and a width of 16.4 mm, and poly-carbonate windows. The drum is driven by a programmable rotary stage (Zaber X-RSB120AD), allowing operation at very precise rotation speeds. The device is illuminated from the back, with a diffuse window at the back of the drum to ensure that the light is distributed on the whole drum surface. A camera (Basler acA2440-75uc) placed at the front of drum takes pictures with a good contrast between the powder, appearing in black, and the air appearing in white due to the light, in a process called “shadowgraphy”.

A coil exchanger with a liquid nitrogen circulation is placed around the drum, and slight contact is made between these two elements. The exchanger is equipped with resistors to control the temperature. With this setup, we are able to test temperatures starting from 90 K. Note that this is relevant for Europa and at least for the hot spots at the South Pole of Enceladus, where temperatures are higher than the rest of the surface (the global surface itself is colder than our experimental temperatures). First, we are limited by the liquid nitrogen at ~ 77.4 K used to cool the system down, meaning we can not go lower than this temperature. Second, we are working under Earth atmosphere containing a lot of oxygen, that becomes liquid around 90 K. To avoid any liquid formation in the drum sample space that would lead to a drastic modification of the behaviour of the powder due to capillary forces, we need to run the experiments above the liquefaction temperature of oxygen. On the other hand, for the two ice powders tested in this work, above 155 K the cohesion was strong enough to lead to the formation of big ice aggregates and sticking of ice to the walls of the drum, a behaviour preventing any useful measurement of any interesting parameter. For all these reasons, we decided to perform our experiments between 90 and 155 K.

The whole experiment is placed in a cold chamber at 248 K, and the sensitive elements of the setup, such as the motor, the light source and the camera, are enclosed in sealed boxes and heated to prevent any damage. The cold chamber is dryer than the experiment room, and to prevent moisture, to avoid any contamination of our samples, we built a box around the device to isolate it from the outside, and we place silica-gel beads inside this box to absorb residual water vapour.

We control the temperature of every element of the experimental setup, first the motor and camera with thermocouple probes to make sure that they are working under good conditions. We measure the temperature inside the drum with a Pt100 probe placed inside the brass body of the drum, and we consider this value as the temperature of our sample inside the drum.

2.3.3. Data acquisition and analysis

Each experimental run consists of several acquisitions at different temperatures for a single sample over a day. The experimental protocol is always the same for every sample. The first phase is a cooling phase, during which the empty drum is put inside the nitrogen circulation system. A pump circulates the liquid nitrogen at maximum flow rate during this phase, to cool down the drum as quickly as possible. During this first experiment step, the sample is kept at very low temperature in liquid nitrogen, in an atmosphere saturated with gaseous nitrogen to avoid any contamination by atmospheric moisture.

Once the drum reaches its minimum temperature, around 93 K, we load the sample by removing the drum from the motor and the cooling system. The drum is opened, loaded and closed in the same cold and nitrogen saturated atmosphere as where the sample is stored. It is then placed back on the motor and the cooling system, to cool it down again to its minimum temperature. The whole loading sequence has to be quickly executed, no more than a few minutes, to avoid as much as possible any atmospheric contamination, and to limit the heating of the whole system.

When the temperature in the drum is stable again, the actual acquisition sequence begins. The first step is to achieve a steady temperature level to perform a measurement. To do so, we regulate the liquid nitrogen flow rate with a needle valve to limit its cooling effect, and use the heating resistors to heat the drum and achieve a balance between cooling and heating. Once we reach a stable temperature, we launch the image acquisition sequence to measure the statistics of the surface slope angles. We first perform a high rotation speed cycle, corresponding to $Fr = 10^{-2}$ or $\Omega = 16.7$ RPM, to put the material in motion and break the eventual previous aggregates. We then perform five rotation speeds, corresponding to $Fr = 1.0 \times 10^{-4}$, $Fr = 5.0 \times 10^{-4}$, $Fr = 1.0 \times 10^{-3}$, $Fr = 5.0 \times 10^{-3}$ and $Fr = 1.0 \times 10^{-2}$ (typical Froude numbers for slumping to cascading regimes for non-cohesive powders, corresponding respectively to $\Omega = 1.67$ RPM, $\Omega = 3.74$ RPM, $\Omega = 5.29$ RPM, $\Omega = 11.82$ RPM and $\Omega = 16.72$ RPM). For each rotation speed, the drum performs 10 rotations, during which we acquire 50 images of the powder, with the time between each image scaled with the rotation speed.

We have to point out here the difficulty to precisely repeat a measurement regarding our experimental device, both considering the sample loading procedure or the temperature stabilisation inside the drum. It is critical for the whole experiment to thermally disturb the sample as less as possible by limiting interactions with it and keeping it at very low temperature. It means that we load the sample without precisely controlling the amount of powder introduced inside the drum, which can lead to different filling degree of the device (between 30 and 60 %). It is also difficult to precisely constrain the temperature inside the drum, meaning that the same heating parameters and liquid nitrogen flow rate will lead to different temperature stabilisation, depending on external conditions. Thus, it is difficult to achieve the exact same temperature stabilisation between different runs, which prevents us to estimate error bars or uncertainties in this work. It is worth noticing that despite these issues, different measurement runs always lead to the same trend with respect to temperature, and clearly show the effect of the grain size (see Sec. 3.3), meaning that our results are relevant.

Once the images have been acquired, an approximation of the angle of the surface is obtained with a “centroid method”, which consists in comparing the center of mass (COM) of the area occupied by the powder on the image to the centre of the drum itself, as illustrated in Fig. 4. We draw a line between these two COM, and the perpendicular to this line, shown in blue on the Fig. 4, represents an average profile of the powder inside the drum, from which we can easily extract an angle α , considered here as the angle of the flowing surface. This angle is corrected from the eventual tilt of the camera by using a vertical reference taken at the beginning of the experiment. We extract this angle for the 50 images we have for each rotation speed, and take the average of these angles as the actual value of the angle of the flowing surface for the considered rotation speed. In a first approximation, we then estimate the variability of the angle of repose by calculating the standard deviation around this mean angle. This second parameter is useful to quantify the cohesion, because by definition a weakly cohesive powder will display a very stable flowing surface (except for

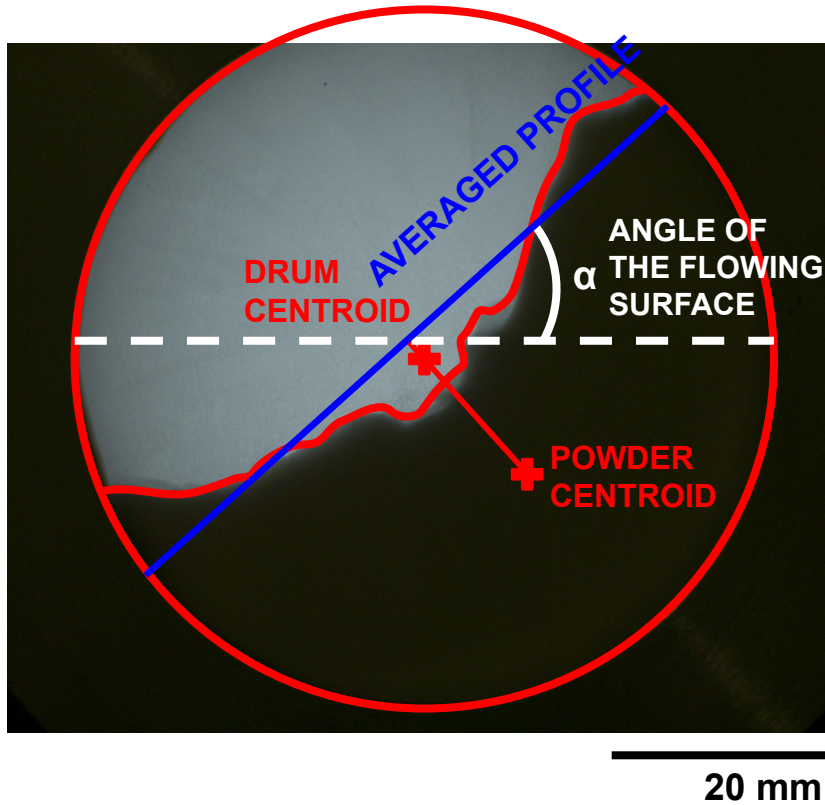


Figure 4: Example of an image acquired with the rotating drum device, and illustration of the “centroid method” applied on this image.

very low rotation speeds). For cohesive powders, the flow will occur by the mean of successive avalanches inside the drum, meaning that between two avalanches the powder will behave as a solid. The extreme angles at which the powder will form an avalanche or stabilise will depend on the actual cohesion of the powder, meaning that a more cohesive powder will display a wider range of possible angles, leading to a higher standard deviation around the mean angle of the flowing surface.

It is important to mention here that there is no standard established method to analyse the data extracted from the drum device, even though this device is a classical geometry in the granular media research field, and is also used as a powder characterisation technique. The angle of the flowing surface is most frequently the parameter of interest, but its estimation and its analysis can differ from one study to the other. Some studies, such as Lumay et al. (2012) or Neveu, Francqui and Lumay (2022), are based on the extraction of the powder flowing profile, but others will prefer the estimation of the angle through the analysis of the centroids as performed in this work, such as Pachón-Morales, Colin, Casalinho, Perré and Puel (2020).

3. Results

3.1. Tests on non-icy reference powders - weakly and strongly cohesive cases

As a first step in the campaign, we ran some experiments on our two reference powders, the limestone powder (considered as strongly cohesive) and the glass beads (considered as weakly cohesive), at very low temperature to get as close as possible to the experimental conditions used for the ice powders, and at all the considered rotation speeds. The images of these experiments have been processed with the “centroid method” (see Sec. 2). Some results of these validation runs are shown on Fig. 5a-b.

As expected, we see a very clear difference in terms of centroid angle between the strongly cohesive and weakly cohesive powder. The cohesive powder tends to have higher angles of the flowing surface, independently of the rotation

Cohesive properties of ice powders

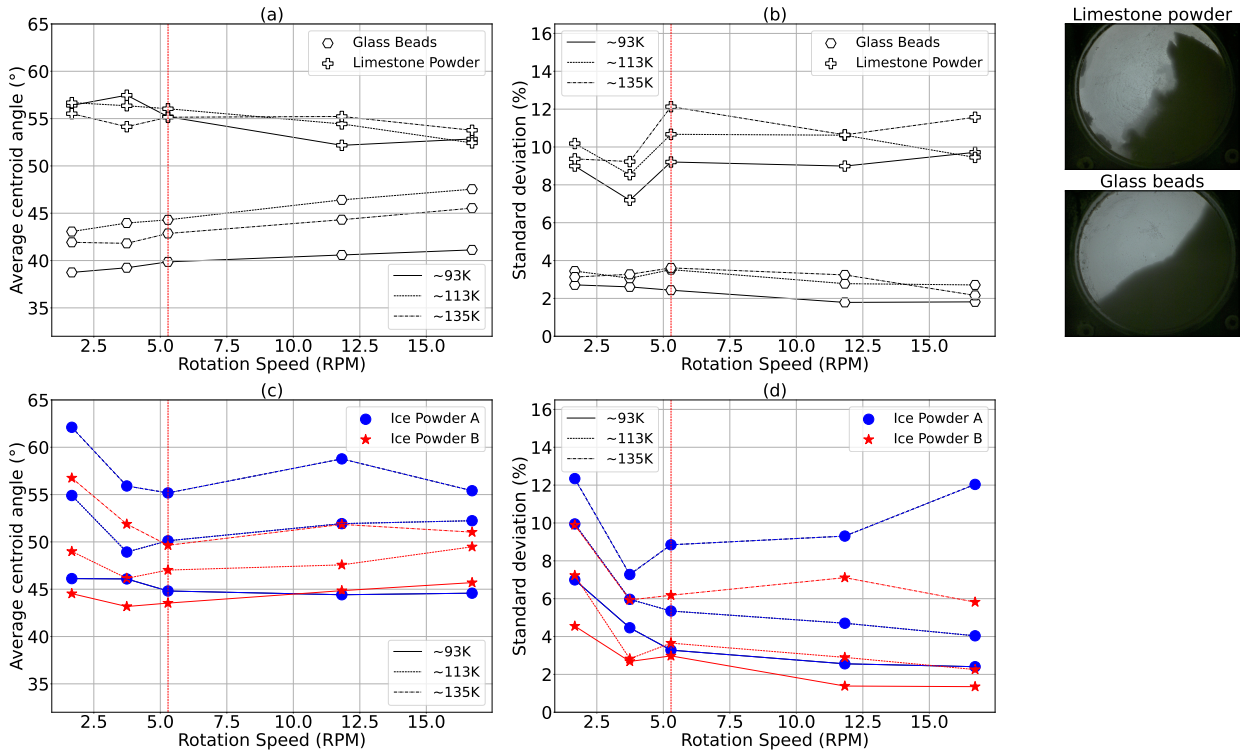


Figure 5: Evolution of the centroid angle and the standard deviation around this angle as a function of the rotation speed for the reference powders (a-b) and the ice powders (c-d), and for different temperatures (~ 93 K, ~ 113 K and ~ 135 K).

speed (or the temperature). For the glass beads, we see a slight increase of the angle with the highest rotation speeds, as expected from Mellmann (2001), but this behaviour is not visible for the limestone powder because of its cohesive nature that erases all the classical regimes usually observed.

Taking a look at the standard deviation (normalised to the average angle), we still see this clear distinction between the two types of powders. For all the rotation speeds (or temperatures), the cohesive powder shows higher values of the standard deviation, meaning that the surface flow is more irregular, more discontinuous than the weakly cohesive powder. We also see a slight decrease of the standard deviation with the rotation speed for the glass beads, showing once again an expected behaviour previously described: the flow becomes more regular with the increasing speed, thus decreasing the variations of the surface angle.

In order to determine the relevance of our rotating drum device, it can be interesting to compare the results obtained for our reference powders to values from literature. The comparison can be made on the average angle of the flowing surface, which is a common parameter. Unfortunately, as there is no universal reference powder in the powder characterisation community, it is difficult to find angle values for the exact samples we used in our experiments. We can, however, look at the flowing behaviours of similar powders with different levels of cohesion.

It is well known in the powder characterisation community that, in a rotating drum device, the average angle of the flowing surface increases with the rotation speed of the drum for a cohesionless material, while it decreases with the speed for a cohesive one (Castellanos, Valverde, Pérez, Ramos and Watson, 1999). In a recent study, Neveu et al. (2022) compared two powders, a cohesive one, made of lactose grains with a size distribution around $40\ \mu\text{m}$, and a non cohesive one which is composed of glass beads with a size distribution around $400\ \mu\text{m}$. They measured the angle of the flowing surface for these two samples for rotation speeds ranging between 2 and 60 RPM, which correspond with their device (their drum being 84 mm in diameter) to Froude numbers between $Fr = 1.9 \times 10^{-4}$ and $Fr = 1.7 \times 10^{-1}$. They found that for their non cohesive powder, the angle was increasing with the rotation speed, from 25° to 55° . For our glass beads sample, for Froude numbers between $Fr = 10^{-4}$ and $Fr = 10^{-2}$, we found the same behaviour, but with higher angles, from 40° to 50° (Fig. 5a). The angle difference observed here between these glass samples may be due to the grain size difference, which is way smaller in our case, and causes our sample to be slightly more cohesive.

Considering the cohesive powders, even if the two samples are different, their behaviour is also quite similar. Neveu et al. (2022) found globally higher angles at low rotation speeds for lactose powder than for glass beads, with a decreasing trend with the rotation speed, from 55° to 45°. Fig. 5 shows the same behaviour for our limestone powder, higher angles than the glass beads, and the angle is slightly decreasing with the rotation speed.

With these first simple measurements, we demonstrated that we can differentiate powders by their level of cohesion from the rotating drum experiment with the determination of the centroid angle (its average value and its standard deviation). Both the mean flowing surface angle and the standard deviation are relevant to characterise the cohesion of a powder in rotation inside a drum. In addition, the rotation speed does not show a strong effect on cohesive powders, which suggests that the method is robust. For the reference powders, we also do not see a clear dependence of the evolution of the angle and its variations with the temperature. It is worth noticing, however, that the curves corresponding to the evolution of the angle for the glass beads (Fig. 5a) display a significant level of scattering, without a clear dependence with the temperature. This surprising behaviour, especially considering the low cohesion level of this powder, may be due to intrinsic noise of our method. We can not exclude here that a small amount of frost was deposited on the grains, even if this phenomenon has not been directly observed during our experiments.

3.2. Influence of the rotation speed

As mentioned in Sec. 2.3.3, each experiment was repeated with five rotation speeds (Fig. 5). According to Mellmann (2001), the rotation speed of the drum device should have a visible influence on the behaviour of weakly cohesive powders, influence that we noticed before, but this effect is not clear for more cohesive powders, such as the limestone powder we tested. As we anticipate the ice powders to be strongly cohesive, we tried to see if the rotation speed had any influence on the angle and its variations for these specific powders, and this at different temperatures. These results are shown on Fig. 5c-d.

This figure shows that, as stated in Sec. 3.1, the rotation speed does not seem to influence the values of angles or standard deviations for the icy powders. The lowest rotation speed displays a different trend compared to the other speeds. The points at very low rotation speed almost always show higher angles of the flowing surface, and higher standard deviation compared to higher rotation speeds, making these particular points questionable. Indeed, in our experimental protocols, the measurements are taken going from low to high speeds. Between two runs, the powder is sitting in the drum without moving for the whole duration of the temperature stabilisation. This could lead to a consolidation of the powder, and even if we try to prevent such a phenomenon by performing multiple rotations at high speed before each measurement, the first rotation speed we use (the slowest one) could still be affected by this possible consolidation. For this reason, we decided to discard the lowest rotation speed for the rest of the study.

Considering the remaining rotation speeds, as this parameter does not seem to have a strong influence on the behaviour of the cohesive powders inside the drum, we decided to only focus on one speed, for the sake of clarity, for the rest of this study. We chose to present the results for the intermediate rotation speed of $\Omega = 5.29\text{RPM}$ (indicated by a vertical dashed line on Fig. 5) for the following results.

Having proven the robustness of the method, in the following we discuss the cohesion of ice powders as a function of particle size and temperature.

3.3. Evolution of the cohesion of water ice powders with the temperature

We ran several experiments on the ice powder samples, at very low temperature, following the protocol described in Sec. 2. We used the two ice powder types described in Sec. 2.2, called Ice Powder A (IP-A) with a median volumetric grain size distribution around 84 μm , and Ice Powder B (IP-B) with a median volumetric grain size distribution around 134.4 μm . For almost all the runs, we followed an increasing “temperature direction”, meaning that we went from very low temperatures ($\sim 93\text{ K}$) to higher temperatures ($\sim 140\text{--}150\text{ K}$) during the run. Only a few measurement points were taken in the other direction to check the reversibility of the process (see Sec. 3.4).

The first qualitative results obtained from these experiments are coming from visual observation of the powder inside the drum. A quick visual inspection of the ice in rotation shows a cohesive-like behaviour, with no continuous flow visible at any rotation speed, no free-flowing layer at the surface of the powder. The powder flows through multiple avalanches¹, displays a highly irregular surface and none of the classical flowing regimes described for non-cohesive powders are recognisable during the whole process. All these properties tend to indicate that both IP-A and B are strongly cohesive.

¹An animation of a sample of ice powder IP-A flowing inside our rotating drum experiments, at a temperature of $\sim 133\text{ K}$ and a rotation speed of 5.29 RPM, is provided as Supplementary Online Material.

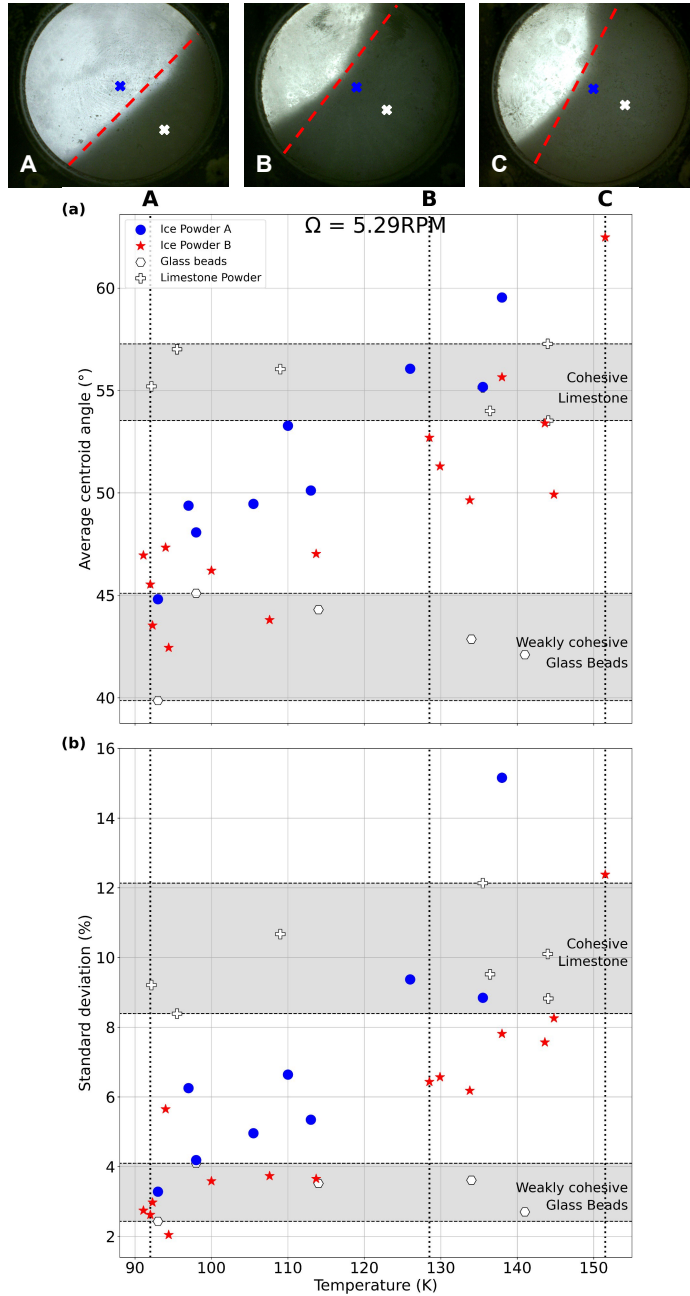


Figure 6: Evolution of (a) the average centroid angle and (b) the standard deviation around this angle with the temperature, for the two ice powder samples and the two test powders. Grey areas represent the weakly-cohesive (glass beads results) and cohesive (limestone powder results) behaviour of powders. The vertical lines indicate the temperature of the examples shown above. Blue and white crosses represent the drum COM and the powder COM, respectively. These examples have all been extracted from Ice Powder B experiments.

Compared to the reference powders showing no systematic dependence with temperature, the two ice powders display a different behaviour. At very low temperature, between 90 and 100 K, the mean angle of the flowing surface is comparable to those of the glass beads, considered as weakly cohesive, for the two icy samples. As the temperature increases, the mean angle increases for the ice powders, to reach the same values as the limestone powder for temperatures around 130-140 K. This behaviour is illustrated in Fig. 6 by the example pictures of ice powder inside

the drum on images A, B and C, corresponding to the different temperatures indicated on the plots. This means that for the considered range of temperatures, the two populations of ice powder display a weakly cohesive behaviour at low temperatures, and a more cohesive behaviour at higher temperatures. However, if the two samples show the same increasing trend for the angle of their flowing surface with the temperature, they seem to display different values of angles. Indeed, for the smaller grains (in blue) the angle is slightly higher than for the bigger grains (in red), indicating a slightly more cohesive behaviour for IP-A.

We see exactly the same tendency in the evolution of the standard deviation with the temperature (Fig. 6b). For the two ice powders, the standard deviation increases with the temperature, indicating that the variations around the mean angle become higher. At very low temperature, between 90 and 100 K, the standard deviation is comparable to the glass beads, and increases to reach values similar to the limestone powder when going up to 140-150 K. Here also, the IP-A samples, the smaller grains, seem to be more cohesive than the IP-B.



Figure 7: Illustration of the ice aggregates formed inside the drum with three individual pictures of the IP-A sample at 143 K. The aggregates are of centimetre-size, hard to break with just a fall in the drum, and no flowing behaviour is observed at this point.

All these results tend to show that both the angle and the irregularities of the flowing surface of ice powders increase with the temperature, which could indicate a global increase of the ice powder cohesion with the temperature. The cohesion increases so much that at temperatures higher than 140-150 K, the ice powder forms centimetre-sized aggregates, like a snowball inside the drum with no flowing behaviour, thus leading to impossible analysis of the slope of the flowing surface with our methods. This phenomenon is observed for temperatures around 150 K, explaining why there is no data points around these values and above. An illustration of this behaviour is displayed in Fig. 7 with three pictures showing the IP-A sample inside the drum device, at a temperature of 143 K, forming macroscopic aggregates and no flowing behaviour. The same behaviour is observed when using very small ice grains. Indeed, we tried to perform the exact same study presented here with a smaller ice grains population (with a median distribution around 20 μm , not presented in this work), but even at very low temperature this sample behaved as a strongly cohesive powder, leading to almost immediate formation of big aggregates, sticking to the windows of the drum, and impossible measurements of any flowing surface.

Knowing the sensitivity of ice to the temperature, we wondered if the effect we saw could be due to physical changes of the grains, such as sublimation/condensation of the smaller grains destabilised by the temperature increase, and could change the shape of the bigger grains, thus changing their flowing properties. We could also have some sintering effect at the contact between the grains, that could lead to the formation of solid bridges between the grains, therefore changing the apparent size of the grains, and the flowing properties of the powder. All these effects would lead to irreversible changes of the powder properties. To eliminate all these assumptions, we run additional rotating drum experiments, with progressive increase and then decrease of the temperature.

3.4. Reversibility of the cohesion evolution

To test the reversibility of the temperature effect, we used the protocol described in Sec. 2.3.3, first going from low temperatures (around 90 K) to higher temperatures (around 140-150 K), acquiring data points as we usually did. To

see if the ice grains actually changed in terms of morphology or properties, we then decreased the temperature and acquired new data points during the descent, to compare these results with the one acquired with the regular protocol.

Fig. 8 shows a hysteresis of both the angle of the flowing surface and the standard deviation, that are both decreasing when the temperature decreases after reaching higher temperatures, even if we do not exactly fall back at the same values of angles. This behaviour is even more remarkable for the standard deviation, for which we seem to follow exactly the same path for the temperature descent than for the ascent. This behaviour indicates that the changes we observed in the powder properties with regular experiments are in fact reversible, and they should not be due to a physical change of the grains such as sublimation or sintering. This confirms that the trend observed on Fig. 6 is due to the intrinsic change of temperature of the grains i.e., is due to a temperature dependence of the particle surface energy.

We also checked that the sample was not altered during this comparative cycle by observing the grains with the optical microscope before and after the experiments. No difference was noticed.

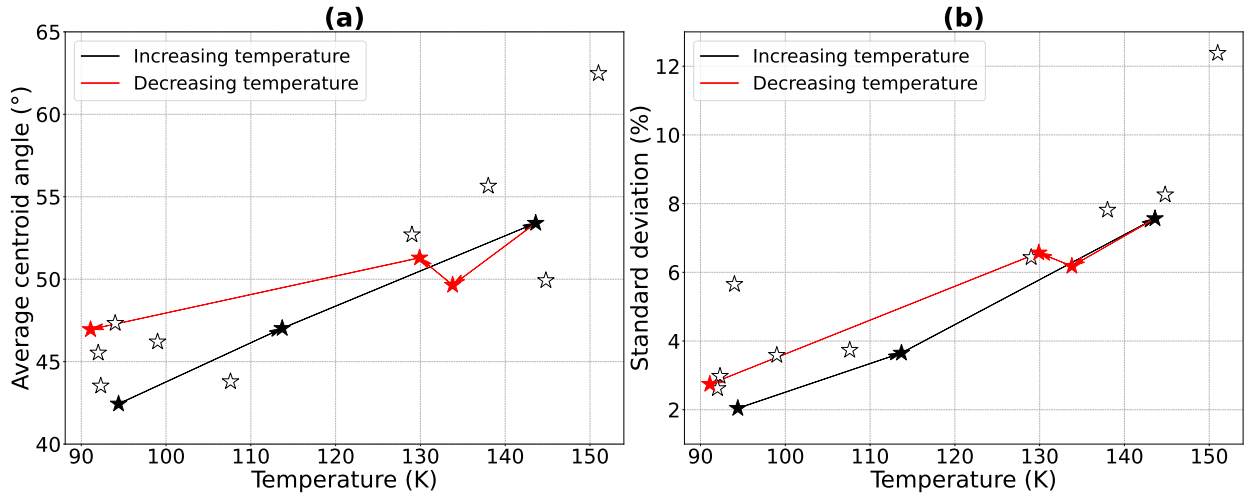


Figure 8: Evolution of (a) the angle and (b) standard deviation of the flowing surface of the powder with the temperature for all the IP-B runs. The results are shown for an intermediate rotation speed of $\Omega = 5.29$ RPM. The filled symbols indicate the back and forth experiment described in Sec. 3.4.

4. Discussion

4.1. Comparison with previous studies

In this work, we investigated experimentally the mechanical behaviour of ice powders at different temperatures with a rotating drum device, in order to determine their cohesive properties. Our experimental results show a clear temperature dependence of the ice cohesion for a temperature range between 90 and 150 K. Increasing the temperature above 150 K resulted in a drastic change of these powders cohesiveness, making the measurements of the cohesion using a rotating drum impossible. Tests performed on samples with smaller grains ($< 20 \mu\text{m}$, not shown here) have revealed an elevated cohesion already at temperatures as low as 90 K, making rotating drum measurements irrelevant. Comparable temperature-dependent behaviour of icy materials were also observed by Musiolik and Wurm (2019) and Gundlach and Blum (2015), but at higher temperatures (> 170 K). At lower temperature, < 150 K, Haack, Otto, Gundlach, Kreuzig, Bischoff, Kührt and Blum (2020) performed tensile strength measurements on a variety of powdery mixtures, including pure water ice powder with a grain size distribution around $2.38 \mu\text{m}$, and they deduced a cohesion value in agreement with previous studies (see Sec. 4.2). We also observed a grain size dependence in the cohesion of our samples, with smaller ice grains being more cohesive, which is an expected behaviour in powdered materials (Mandal, Nicolas and Pouliquen, 2020).

Previous studies suggested that this temperature dependence of cohesion was due to some surface processes, possibly due to a modification of strength of the hydrogen bonds between ice particles, which may be the dominant interactions to explain the intensity of the cohesion, or even, in less extent, Van der Waals interactions. Choukroun et al. (2020) performed sintering experiments on ice powders, and deduced that sintering processes (i.e. the formation of

solid bridges at the contact between ice grains) could also take place with sufficient time, depending on the temperature. Sintering processes would lead to an increase of the penetration resistance and changes of the apparent physical properties of the material, but the coldest the powder is, the less resistance it will build within the same duration. At 193 K, Choukroun et al. (2020) found that a sample of ice powder builds a resistance of 2-3 MPa in 400 days. They deduced that under Enceladus surface conditions, little to no strengthening of plume deposits is expected. Even on the South Polar Terrain, near the Tiger Stripes, they estimate that at least the age of the Solar System is required to build a resistance of around 1 MPa. Another hypothesis is linked to the existence of a quasi-liquid layer of water at the surface of ice grains, forming even well below the melting point of water ice (Rosenberg, 2005). This layer is used to explain the slippery behaviour of ice, but in our case it could be involved into some capillarity effects at high temperatures. Indeed, according to Döppenschmidt and Butt (2000), this layer is very thin, a few dozens of nanometers, and behaves as a liquid when two surfaces are in contact. But the thickness of this layer is also decreasing when the temperature drops, meaning that we should lose some capillary forces, maybe explaining the changes observed inside our drum. This link is not straightforward though, because according to Döppenschmidt, Kappl and Butt (1998) this melted layer only appears consistently around 240 K, which is at least 90 K higher than the temperatures we investigated. However, they ran their experiments on compact ice layers with a thickness of 0.5 mm, which may not be affected by this liquid-like layer in the same way as our microscopic grains.

Future work is required to better understand this process at the microscopic scale with a study of this behaviour through an infrared spectrometer, to investigate eventual changes in the molecular bonds or vibrations that could explain this increase of cohesion with the temperature. According to Kahan, Reid and Donaldson (2007), it might be possible to probe the properties of the quasi-liquid layer at the surface of our ice grains using Raman spectroscopy, which could be part of a future study to investigate in more details this phenomenon.

4.2. Estimation of the surface energy of ice

To better characterise the temperature dependence of the powder cohesion of ice and its extrapolation to a wide range of temperature and grain size, we derived a simple dimensional analysis relating the powder cohesion and other forces acting on the material, notably body forces, as classically done in the granular materials field (Castellanos, 2005). At the particle scale, one usually defines a dimensionless number called the Bond number, which is the ratio between interparticle cohesive forces and particle weight:

$$Bo = \frac{F_{cohesion}}{F_{gravity}} = \frac{6\gamma}{\rho_p g d^2}, \quad (2)$$

where γ is the surface energy of the material, ρ_p the material density, g the gravity, d the particle size. The case $Bo = 1$ corresponds to the combination of parameters for which cohesion is able to sustain the weight of a particle. Note that at a macroscopic scale it may be more relevant to consider continuum level stresses instead of particle scale forces, and therefore to compare the cohesive yield stress σ_c in the bulk of the material to the weight of a portion of material of characteristic depth h . This allows the introduction of a macroscopic Bond number defined as :

$$Bo_M = \frac{\sigma_c}{\rho g h} = \frac{\gamma}{\rho_p g h d}, \quad (3)$$

where $\rho = \rho_p \phi$ is the bulk density, where ϕ is the solid volume fraction, and use has been made of the expected scaling of cohesive stress with particle size : $\sigma_c \sim \phi \frac{\gamma}{d}$ (Mandal et al., 2020). Whether one or the other dimensionless parameter is more relevant, it depends on the application. Both parameters comprise the variables which are expected to influence the effective cohesion of the powder. Decreasing particle size, gravity or particle density contribute to increase the importance of cohesive forces. The effect of temperature observed in our experiments has therefore to be assigned to the surface energy of the material.

To highlight the effect of the temperature on the effective surface energy of ice particles, we scaled our experimental data using a simple avalanche model inside a rotating drum device. The objective here is to derive an expression of the surface energy of the powder that is independent of the size of the system, the gravity, or all other external forces. This derivation exercise is presented in A, and introduces the simple avalanche model we used in Fig. A.1, which depicts the failure of the powder inside the drum (middle sketch). Only the final equations are presented here.

Doing this approximation, the surface energy γ can be scaled as:

$$\gamma = \frac{4 \rho_p g d R_{drum}}{9 Z \sin \delta} \left[1 - \cos(4\sqrt{3}\sigma_\theta) \right], \quad (4)$$

where ρ_p is the intrinsic density of the material, g the gravity, d the diameter of the particles, R_{drum} the radius of the drum, Z the coordination number (the average number of contacts per grain), δ the internal angle of friction and σ_θ the standard deviation around the average angle of the flowing surface inside the drum. As stated in Appendix A, a reasonable value for δ should be around 30° . For the coordination number Z , we took a value of $Z = 5$.

These values, injected into the Eq. 4 give the evolution of the surface energy of all our samples between 90 K and 150 K, as illustrated with Fig. 9. This figure confirms the trend previously seen with raw data points, with a clear increase of the surface energy with the temperature for the two ice powder samples. On the other hand, the two model powders (limestone and glass beads) show no dependence to the temperature. Even if the glass beads display a less cohesive behaviour than the limestone powder, the parameter γ of such materials seems very close. The limestone powder displays a higher value of surface energy than the glass beads, but such a difference can not explain the difference of behaviour observed during the experiments. This is therefore certainly due to the grain size, which is way smaller for the limestone powder ($\sim 17 \mu\text{m}$ for limestone powder, while it is $\sim 36 \mu\text{m}$ for glass beads). It means that the limestone grains are more efficiently affected by the cohesion forces.

With this figure, we also see that the surface energy of ice particles is comparable or smaller than the test powders at very low temperature, but becomes higher for the highest temperatures. Interestingly, the slight difference we could previously observe between the powders is still visible but with a way smaller amplitude, as here the cohesion parameter should be less dependent of the size of the particles we have in the system.

Musiolik and Wurm (2019) found a value of $\gamma_{ice} = 0.0079 \text{ J.m}^{-2}$ at 175 K, which is comparable to our own values for γ_{ice} when we extrapolate our fit to similar temperatures (see Fig. 9). Below 150 K, Haack et al. (2020) found a value of $\gamma_{ice} = 0.0026 \text{ J.m}^{-2}$, which is in good agreement with our own experimental results, even though their temperature measurement is not as precise as ours.

Remarkably, our data points seem to follow an exponential law depending on the temperature. If we actually assume an exponential law for our data points, we can use the Arrhenius equation to make the link between the cohesion γ , the temperature T and an activation energy Q . The fitted curve shown on Fig. 9 reproduces quite well the obtain results for ice powders, and leads to an equation of the surface energy γ :

$$\gamma = 0.17 e^{\frac{-Q}{RT}}, \quad (5)$$

with Q the activation energy, R the ideal gas constant $8.314 \text{ J}/(\text{mol.K})$ and T the temperature. This fit gives a value of $Q = 4.6 \pm 0.3 \text{ kJ.mol}^{-1}$, which is low compared to other studies performed at higher temperatures like for instance, Choukroun et al. (2020) (they found $Q = 24.3 \pm 3.3 \text{ kJ.mol}^{-1}$), but their work was focused on the sintering processes occurring at the contact between the grains. This further confirms that the observed change of cohesion in our samples is not due to sintering processes, consistent with our reversibility experiment tests (see Sec. 3.4).

4.3. Implications for the icy moons of Jupiter and Saturn

Our results imply that the mechanical properties of fresh deposits may significantly vary in space and time at the surface of Europa and Enceladus, even before they become consolidated due to sintering processes (Choukroun et al., 2020), which would take more than 10,000 yrs at temperatures below 150 K. On Europa, the mean annual temperature is around 100 K, but it can vary from around 80 K during nighttime up to around 130 K at the equator at noon (Spencer, Tamppari, Martin and Travis, 1999). As seen with our experimental results, the cohesion of ice powders is highly dependent of the temperature (see Sec. 4.2) over that temperature range. Similarly on Enceladus, the temperature typically varies from about 70 K far from Tiger Stripes to more than 150 K at the vicinity of the warmest part of the fractures (Spencer, Nimmo, Ingersoll, Hurford, Kite, Rhoden, Schmidt and Howett, 2018).

Fig. 10b shows the evolution of the Bond number as a function of both temperature and grain size, calculated with Eq. 2, using the expression of the surface energy given by Eq. 5 for both Europa's and Enceladus' gravity. For grain sizes between a few tens to hundreds of micrometres (corresponding to the typical grain sizes used in our experiments), we obtained Bond numbers comparable to the values explored in our experiments. This means that on Europa, for grains similar to the experimental ones, we could expect the ice powders to behave in the same way as in our most cohesive experiments. This map implies that, at all temperatures between 80 and 130 K, fresh ice deposits on Europa will behave

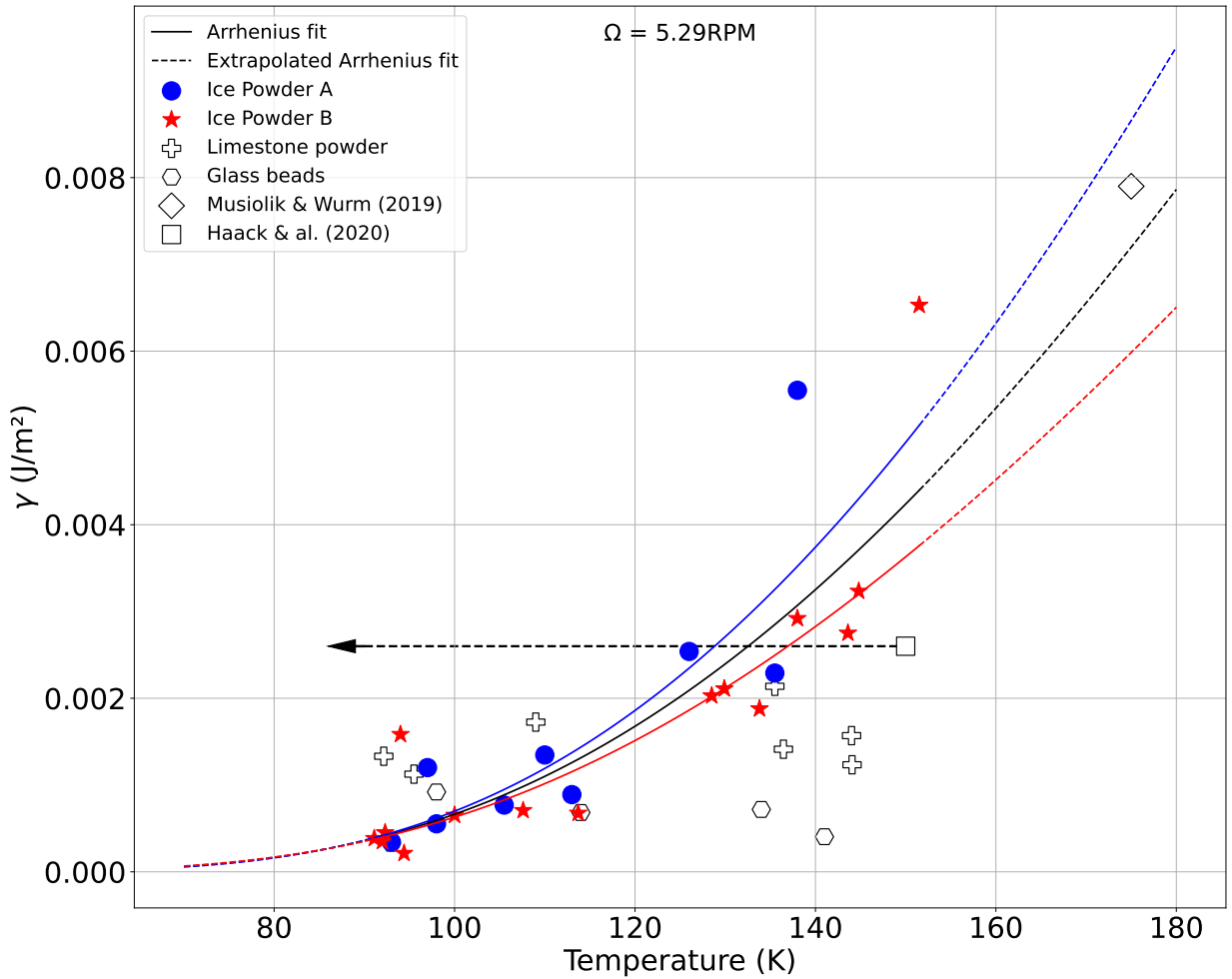


Figure 9: Evolution of the surface energy parameter with the temperature for all the tested powders. The experimental results of Musiolik and Wurm (2019) and Haack et al. (2020) have been added to the plot.

as cohesive powders for grain size smaller than 100 μm , and would get only weakly cohesive for grain sizes exceeding a few hundred microns.

Interestingly, based on Bond number predictions (Fig. 10b), for grain size of the order of 100-300 μm , the ice powder should vary from weakly to strongly cohesive behaviour for temperatures ranging between 80 and 150 K. Knowing the temperature variations at the surface of Europa, this means that different regions display different cohesion levels. For example, ice powders at the poles that are colder (~ 80 K) will be less cohesive than the same powder at the equator. Similar behaviour is expected with the daytime cycle. For instance a material with a grain size of about 100 μm deposited around the equator will behave during daytime as a highly cohesive material, and will be able to build very loose structures, with a very high porosity (Capece, Huang, To, Aloia, Muchira, Davé and Yu, 2014) and strong slopes (Lumay et al., 2012). But during nighttime, the temperature drops, and the cohesion of this material decreases, leading to possible destabilisation of the powder even with a small perturbation.

Mills, Pappalardo, Panning, Leonard and Howell (2023) studied the effect of moonquakes triggered by tidal deformations on the stability of icy granular materials at the surface of the icy moons. They inferred a quake magnitude range of 4.0-7.9 which, according to their models, is enough to trigger the destabilisation of a granular material, and thus causing mass wasting of icy regolith. For weakly cohesive powder, mass destabilisation could occur at even lower quake magnitude. As the cohesion should vary at different locations and time on Europa, the energy required to destabilise the material and produce a granular flow would also change. This particular behaviour may explain flow-like features

observed in various locations on Europa's surface and smooth material filling some topographic lows, for instance on the flanks of double ridges (Prockter and Patterson, 2009; Quick and Hedman, 2020) or various lobate features identified as cryovolcanic sites (Lesage, Schmidt, Andrieu and Massol, 2021). This would also have some important implications regarding the erosion of steep slopes by successive flows. Moreover, the reduction of ice cohesiveness with decreasing temperature should also help the flow of freshly eruptive granular ice materials at the surface, potentially providing an explanation for the numerous flow features observed at Europa's surface, whose morphology implies the existence of a very low viscosity fluid (Miyamoto, Mitri, Showman and Dohm, 2005). Partially molten ice slurries should rapidly freeze as the flow is progressing, thus limiting the flow rate, while granular ice powder will keep a good flowability, which further increases with decreasing temperature. Future modelling work will be needed to test the efficiency of powder flow on Europa's surface and the effusion rate required to explain the observed flow features.

On Enceladus, the temperatures are lower than at the surface of Europa, ranging from around 50 K at the poles to around 80 K at the equator at noon time (Howett, Spencer, Pearl and Segura, 2010). However, Spencer and Nimmo (2013) estimated temperatures as high as around 180 K at some locations on the Tiger Stripes at the South Polar Terrain. Fig. 10a shows that, for grain sizes smaller than 100 μm , the predicted Bond number is much larger than the highest value reached in our experiments, implying a very cohesive behaviour for the ice powder, independent of the temperature comprised between 70 and 180 K. This means that everywhere at the surface the fresh deposited regolith is able to build very loose structures with high porosity. The cohesion is largely able to sustain the weight of multiple particles, which means that without any external perturbation, the cohesion will keep the porosity at very high values. Because of this property, the cohesion of ice grains could easily build a regolith with a very high thickness at the surface of Enceladus. This property of Enceladus' regolith have been studied by Martin et al. (2023), and they deduce that the regolith could be as thick as 700 m at some locations on Enceladus. They explain this important thickness by a higher deposition rate than previously established, but also by a very high porosity of the deposited material that we could explain with ice powder cohesion. At the vicinity of the active faults in the south polar terrain, because of the higher temperature, freshly deposited ice powder should always display a more cohesive behaviour than on the rest of the moon, but according to Fig. 10 even at temperatures as low as 60-70 K, ice powder should have a cohesive behaviour, for grain sizes smaller than 100 μm , due to the weak gravity.

The cohesion of the icy regolith is not expected to be constant everywhere at the surface of Enceladus because of temperature variations, but also because of the plume activity. Indeed, the deposition rate of the ejected material is not the same at every place of the moon. Kempf et al. (2010) and Southworth et al. (2019) studied the deposition rates and maps at the surface of Enceladus. They estimated that the larger grains had a lower velocity, and they were more easily falling back at the surface and closer to the Tiger Stripes. This would mean that the average grain size is larger close to the Tiger Stripes, consistent with VIMS data (Jaumann et al., 2008; Taffin et al., 2012), leading to a competition between temperature and size effects. The material deposited close to the stripes is less cohesive because of its grain size, counteracting the effect of the temperature. On the other hand, grain velocities have also been estimated to be around 200 $\text{m}\cdot\text{s}^{-1}$ at the exit of the vent, and in the absence of atmosphere they are not slowed down when they fall back, meaning they collide with the surface with about the same velocity. It is difficult to know what would be the effect of such high velocity impacts, but we can expect that if the grains fall on a very cohesive and loose structure, they could be able to break the cohesive bonds between the grains. This could cause a reorganisation of the grains, a decrease of the porosity and then a dynamic compaction process. Further modelling work is needed to investigate the effect of particles falling on the powder structure and its consequences for the macroscopic cohesiveness.

Due to the difference of gravity between Europa and Enceladus, two identical ice powders will not display the same behaviour on their surfaces, as indicated from the difference in Bond number for similar grain sizes and temperatures on the two moons (Fig. 10). Due to a smaller gravity, the surface porosity on Enceladus would always be higher than on Europa for a given grain size and temperature. High cohesion and low gravity can result in a very low compressive strength of the surface materials, similar to what has been experienced by *Philae* upon landing on the comet 67P/Churyumov-Gerasimenko (O'Rourke et al., 2020). Such a very low compressive strength may make the landing more challenging, or at least requires specific landing designs. Future work is required to link the spectral and morphological signatures to the surface material cohesion and strength, in order to identify the best sites for safe landing for future missions. Considering the sampling part of a mission of this type, the highly cohesive nature of the material would probably make it easy to detach from the surface because of its porous nature. However, the adhesive nature of the grains would maybe make them difficult to analyse, because they could stick to the sampling tool, or stick to each other, making them difficult to separate for individual analyses. Future experimental tests on analogous

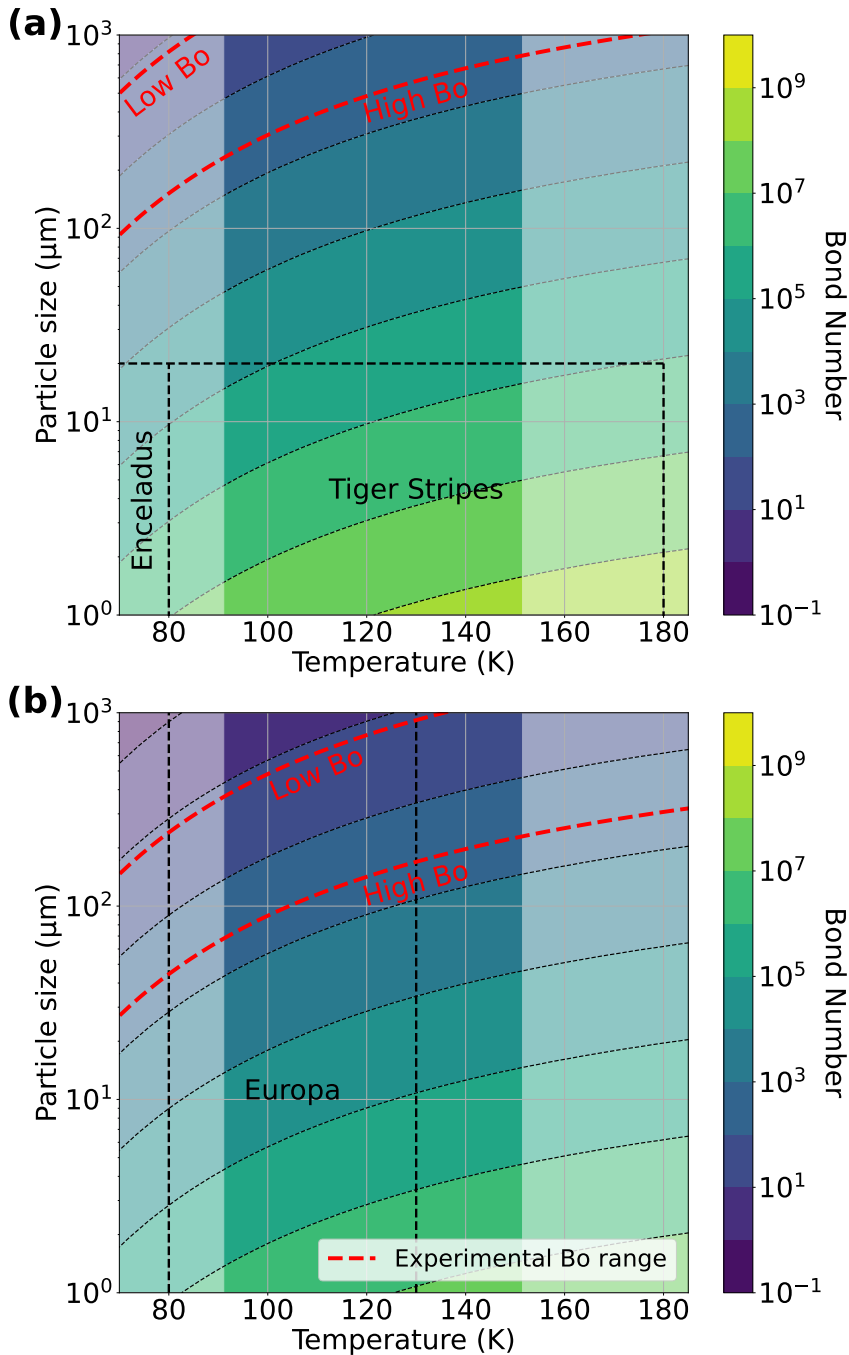


Figure 10: Maps of the Bond Number as a function of the temperature and the grain size calculated for the case of (a) Enceladus' gravity, and (b) Europa's gravity. The highlighted area corresponds to our experimental temperature range. On both maps, the temperature ranges of the different interesting bodies have been indicated, as well as the grain size ranges when possible. The red dotted lines correspond to the range of Bond numbers covered by our experimental results, from $Bo \sim 13.9$ to $Bo \sim 405.4$.

powders of various grain size, temperature, and composition will be useful to determine the best sampling and analysis technique.

5. Conclusion

In this experimental work, we developed a cryogenic rotating drum to study the flow ability of ice powders, and found as a striking result that the cohesive behaviour of ice powders strongly varies for temperatures ranging from 90 to 150 K. This was quantified by means of the statistics of the angle of the flowing surface of ice powders, and its variations, with temperature, a process that is reversible and that shows an important change of cohesion of the material. From a simple model of avalanche occurring inside a rotating drum device, based on the characteristic double slope observed in our experiments, we were able to link the geometry of the powder flow, represented by the standard deviation around the average angle of the flowing surface, to the surface energy of the material, corresponding to the cohesion. We showed a clear relationship between the cohesion of ice powders and the temperature, with an exponential increase of the surface energy with temperature, which is not the case for other, more common powders, which we used as a reference. The values estimated for the ice powder, particle scale surface energy, are in agreement with previous studies, and both our icy samples follow the same trend, independently of their grain size.

The increase of cohesion with temperature is of particular interest in the context of the icy moons surface conditions. By the use of a dimensionless number, the macroscopic Bond number, we were able to compare the importance of the cohesion to the gravity, to place our samples in the context of icy regoliths. We were able to determine that for any relevant temperature at the surface of Europa or Enceladus, or for any characteristic grain size of these bodies, the gravity is weak enough for the cohesion to have an controlling effect. This means that the ice powder at the surface will always behave as strongly cohesive, and will be able to build a thick regolith with potentially high porosity, especially around warmer spots such as the Tiger Stripes at the South Pole of Enceladus. This result is of particular importance for the potential future landing mission for which such a porous and fluffy surface layer will be challenging for landing.

We also highlight an interesting cyclic effect that can be mentioned here, with the day-night cycle that changes the surface temperature, and thus the cohesion of the ice powder at the surface. This means that freshly erupted icy powder could become more or less flowable depending on the time of the day, and such variations could lead to mass wasting or granular flow at the surface. Variations in the cohesion of such materials could also be used to explain some flow features observed at the surface, difficult to explain by regular models of eruptions of liquid fluids.

The results we reported here on pure ice powders are particularly relevant for Enceladus, where relatively pure ice grains are continuously erupted at the South Pole. To address other icy moon conditions, new developments are currently ongoing to perform measurements on more complex analogues, such as ice powders made of angular grains, salty ice powders, or mixtures of ice grains and rocky or organic grains. It is crucial to understand the mechanical behaviour of such samples, as they represent better planetary analogues than pure ice powders, and they are characteristic of a wider range of icy bodies, with applications to Ganymede, Callisto, Titan, Ceres, Uranus moons or even Mars. Estimating the surface energy of these analogues with the rotating drum device will allow us to access the surface state of these bodies, and a probable link with the temperature, as seen with pure ice, as well as influence of non-icy components. Using ice grains with different geometries, such as bigger diameter or different shapes, is also of great interest to access more parameters that are usually dominated by cohesion, like friction between grains, rolling friction of ice particles, which may be relevant for different icy regolith contexts.

As the rotating drum device may not be relevant for every icy samples, especially the ones that are too cohesive such as ice powders made of tiny grains, or temperatures that are too high, developing complementary experiments could help to fully understand the material, but also to give access to additional mechanical parameters. Shear cell experiments at low temperature with an adapted powder rheometer constitute a technical challenge but could give a more direct access to cohesion.

Spectral characterisation in UV/visible and IR of tested samples will also be very useful to anticipate the interpretation of future data acquired by space missions, and would allow us to connect the spectral signatures to the physical state of ice powders. This will be essential to identify the fresh deposits area at the surface of Europa in the context of the *JUICE* and *Europa Clipper* missions and to re-interpret the data acquired by *Cassini* at Enceladus with objectives of re-assessing the grain size distribution and physical state of plume ice deposits on Enceladus.

Acknowledgements

The present study received financial supports from the project GRIM funded by the Region Pays de La Loire (France) and from CNES for the preparation of the NASA *Europa Clipper* and ESA *JUICE* missions.

References

- Badescu, M., Riccobono, D., Ubellacker, S., Backes, P., Dotson, M., Molaro, J., Moreland, S., Csomay-Shanklin, N., Choukroun, M., Brinkman, A., Genta, G., 2019. Sampling Tool Concepts for Enceladus Lander In-Situ Analysis, in: 2019 IEEE Aerospace Conference, pp. 1–12. doi:10.1109/AERO.2019.8741568.
- Bierhaus, E.B., Zahnle, K., Chapman, C.R., 2009. Europa's Crater Distributions and Surface Ages, in: Pappalardo, R.T., McKinnon, W.B., Khurana, K.K. (Eds.), Europa. University of Arizona Press, p. 161.
- Capece, M., Huang, Z., To, D., Aloia, M., Muchira, C., Davé, R.N., Yu, A.B., 2014. Prediction of porosity from particle scale interactions: Surface modification of fine cohesive powders. *Powder Technology* 254, 103–113. URL: <https://www.sciencedirect.com/science/article/pii/S0032591014000151>, doi:<https://doi.org/10.1016/j.powtec.2014.01.006>.
- Castellanos, A., 2005. The relationship between attractive interparticle forces and bulk behaviour in dry and uncharged fine powders. *Advances in Physics* 54, 263–376. URL: <https://doi.org/10.1080/17461390500402657>, doi:10.1080/17461390500402657, arXiv:<https://doi.org/10.1080/17461390500402657>.
- Castellanos, A., Valverde, J.M., Pérez, A.T., Ramos, A., Watson, P.K., 1999. Flow Regimes in Fine Cohesive Powders. *Physical Review Letters* 82, 1156–1159. doi:10.1103/physrevlett.82.1156.
- Cerubini, R., Pommerol, A., Yoldi, Z., Thomas, N., 2022. Near-infrared reflectance spectroscopy of sublimating salty ice analogues. implications for icy moons. *Planetary and Space Science* 211, 105391. doi:10.1016/j.pss.2021.105391.
- Choblet, G., Tobie, G., Buch, A., Čadek, O., Barge, L.M., Běhouňková, M., Camprubi, E., Freissinet, C., Hedman, M., Jones, G., Lainey, V., Le Gall, A., Lucchetti, A., MacKenzie, S., Mitri, G., Neveu, M., Nimmo, F., Olsson-Francis, K., Panning, M., Postberg, F., Saur, J., Schmidt, J., Sekine, Y., Shibuya, T., Sotin, C., Soucek, O., Szopa, C., Usui, T., Vance, S., Van Hoolst, T., 2021. Enceladus as a potential oasis for life: Science goals and investigations for future explorations. *Experimental Astronomy* 54, 809–847. doi:10.1007/s10686-021-09808-7.
- Choukroun, M., Molaro, J.L., Hodyss, R., Marteau, E., Backes, P., Carey, E.M., Dhaouadi, W., Moreland, S., Schulson, E.M., 2020. Strength Evolution of Ice Plume Deposit Analogs of Enceladus and Europa. *Geophysical Research Letters* 47. doi:10.1029/2020gl088953.
- Döppenschmidt, A., Butt, H.J., 2000. Measuring the Thickness of the Liquid-like Layer on Ice Surfaces with Atomic Force Microscopy. *Langmuir* 16, 6709–6714. doi:10.1021/la990799w.
- Döppenschmidt, A., Kappl, M., Butt, H.J., 1998. Surface Properties of Ice Studied by Atomic Force Microscopy. *The Journal of Physical Chemistry B* 102, 7813–7819. doi:10.1021/jp981396s.
- Fagents, S.A., 2003. Considerations for effusive cryovolcanism on Europa: The post-Galileo perspective. *Journal of Geophysical Research: Planets* 108. doi:10.1029/2003je002128.
- Fagents, S.A., Lopes, R.M.C., Quick, L.C., Gregg, T.K.P., 2022. Cryovolcanism, in: *Planetary Volcanism across the Solar System*. Elsevier, pp. 161–234. doi:10.1016/b978-0-12-813987-5.00005-5.
- Glass, J., Dierssen, H., Glein, C., Schmidt, B., Winebrenner, D., 2022. Defining and Characterizing Habitable Environments in Ocean World Systems. *Oceanography* doi:10.5670/oceanog.2021.414.
- Grasset, O., Dougherty, M.K., Coustenis, A., Bunce, E.J., Erd, C., Titov, D., Blanc, M., Coates, A., Drossart, P., Fletcher, L.N., Hussmann, H., Jaumann, R., Krupp, N., Lebreton, J.P., Prieto-Ballesteros, O., Tortora, P., Tosi, F., Van Hoolst, T., 2013. JUPITER ICy moons Explorer (JUICE): An ESA mission to orbit Ganymede and to characterise the Jupiter system. *Planetary and Space Science* 78, 1–21. doi:10.1016/j.pss.2012.12.002.
- Gundlach, B., Blum, J., 2015. The stickiness of micrometer-sized water-ice particles. *The Astrophysical Journal* 798, 34. doi:10.1088/0004-637x/798/1/34.
- Gundlach, B., Kiliyas, S., Beitz, E., Blum, J., 2011. Micrometer-sized ice particles for planetary-science experiments - I. Preparation, critical rolling friction force, and specific surface energy. *Icarus* 214, 717–723. doi:10.1016/j.icarus.2011.05.005.
- Haack, D., Otto, K., Gundlach, B., Kreuzig, C., Bischoff, D., Kühr, E., Blum, J., 2020. Tensile strength of dust-ice mixtures and their relevance as cometary analog material. *Astronomy & Astrophysics* 642, A218. URL: <https://doi.org/10.1051/0004-6361/202037763>, doi:10.1051/0004-6361/202037763.
- Hand, K.P., Phillips, C.B., Murray, A., Garvin, J.B., Maize, E.H., Gibbs, R.G., Reeves, G., Martin, A.M.S., Tan-Wang, G.H., Krajewski, J., Hurst, K., Crum, R., Kennedy, B.A., McElrath, T.P., Gallon, J.C., 272 authors, 2022. Science Goals and Mission Architecture of the Europa Lander Mission Concept. *The Planetary Science Journal* 3, 22. URL: <https://dx.doi.org/10.3847/PSJ/ac4493>, doi:10.3847/PSJ/ac4493.
- Hand, K.P., Sotin, C., Hayes, A., Coustenis, A., 2020. On the Habitability and Future Exploration of Ocean Worlds. *Space Science Reviews* 216. doi:10.1007/s11214-020-00713-7.
- Hansen, C.J., Esposito, L., Stewart, A.I.F., Colwell, J., Hendrix, A., Pryor, W., Shemansky, D., West, R., 2006. Enceladus' Water Vapor Plume. *Science* 311, 1422–1425. URL: <https://www.science.org/doi/abs/10.1126/science.1121254>, doi:10.1126/science.1121254, arXiv:<https://www.science.org/doi/pdf/10.1126/science.1121254>.
- Hansen, G.B., McCord, T.B., 2004. Amorphous and crystalline ice on the Galilean satellites: A balance between thermal and radiolytic processes. *Journal of Geophysical Research* 109. doi:10.1029/2003je002149.
- Hedman, M.M., Nicholson, P.D., Showalter, M.R., Brown, R.H., Buratti, B.J., Clark, R.N., 2009. SPECTRAL OBSERVATIONS OF THE ENCELADUS PLUME WITH CASSINI-VIMS. *The Astrophysical Journal* 693, 1749–1762. doi:10.1088/0004-637x/693/2/1749.
- Hillier, J.K., Green, S.F., McBride, N., Schwanethal, J.P., Postberg, F., Srama, R., Kempf, S., Moragas-Klostermeyer, G., McDonnell, J.A.M., Grun, E., 2007. The composition of saturn's e ring. *Monthly Notices of the Royal Astronomical Society* 377, 1588–1596. doi:10.1111/j.1365-2966.2007.11710.x.
- Howell, S.M., Pappalardo, R.T., 2020. NASA's Europa Clipper - a mission to a potentially habitable ocean world. *Nature Communications* 11. doi:10.1038/s41467-020-15160-9.
- Howett, C.J.A., Spencer, J.R., Pearl, J., Segura, M., 2010. Thermal inertia and bolometric Bond albedo values for Mimas, Enceladus, Tethys, Dione, Rhea and Iapetus as derived from Cassini/CIRS measurements. *Icarus* 206, 573–593. URL: <https://www.sciencedirect.com/science/article/pii/S001910350900308X>, doi:<https://doi.org/10.1016/j.icarus.2009.07.016>. cassini at Saturn.

- Iess, L., Stevenson, D.J., Parisi, M., Hemingway, D., Jacobson, R.A., Lunine, J.I., Nimmo, F., Armstrong, J.W., Asmar, S.W., Ducci, M., Tortora, P., 2014. The Gravity Field and Interior Structure of Enceladus. *Science* 344, 78–80. doi:10.1126/science.1250551.
- Ingersoll, A.P., Nakajima, M., 2016. Controlled boiling on Enceladus. 2. Model of the liquid-filled cracks. *Icarus* 272, 319–326. doi:10.1016/j.icarus.2015.12.040.
- Jaumann, R., Stephan, K., Hansen, G.B., Clark, R.N., Buratti, B.J., Brown, R.H., Baines, K.H., Newman, S.F., Bellucci, G., Filacchione, G., et al., 2008. Distribution of icy particles across Enceladus' surface as derived from Cassini-VIMS measurements. *Icarus* 193, 407–419.
- Jia, X., Kivelson, M.G., Khurana, K.K., Kurth, W.S., 2018. Evidence of a plume on Europa from Galileo magnetic and plasma wave signatures. *Nature Astronomy* 2, 459–464. doi:10.1038/s41550-018-0450-z.
- Johnson, K.L., Kendall, K., Roberts, A.D., 1971. Surface energy and the contact of elastic solids. *Proceedings of the Royal Society A* 324, 301–313. doi:10.1098/rspa.1971.0141.
- Jost, B., Pommerol, A., Poch, O., Gundlach, B., Leboeuf, M., Dadras, M., Blum, J., Thomas, N., 2016. Experimental characterization of the opposition surge in fine-grained water-ice and high albedo ice analogs. *Icarus* 264, 109–131. doi:10.1016/j.icarus.2015.09.020.
- Kahan, T.F., Reid, J.P., Donaldson, D.J., 2007. Spectroscopic Probes of the Quasi-Liquid Layer on Ice. *The Journal of Physical Chemistry A* 111, 11006–11012. doi:10.1021/jp074551o.
- Kempf, S., Beckmann, U., Moragas-Klostermeyer, G., Postberg, F., Srama, R., Economou, T., Schmidt, J., Spahn, F., Grün, E., 2008. The E ring in the vicinity of Enceladus. *Icarus* 193, 420–437. doi:10.1016/j.icarus.2007.06.027.
- Kempf, S., Beckmann, U., Schmidt, J., 2010. How the Enceladus dust plume feeds Saturn's E ring. *Icarus* 206, 446–457. doi:10.1016/j.icarus.2009.09.016.
- Kuskov, O.L., Kronrod, V.A., 2005. Internal structure of Europa and Callisto. *Icarus* 177, 550–569. doi:10.1016/j.icarus.2005.04.014.
- Lesage, E., Massol, H., Schmidt, F., 2020. Cryomagma ascent on Europa. *Icarus* 335, 113369. URL: <https://www.sciencedirect.com/science/article/pii/S0019103518304834>, doi:<https://doi.org/10.1016/j.icarus.2019.07.003>.
- Lesage, E., Schmidt, F., Andrieu, F., Massol, H., 2021. Constraints on effusive cryovolcanic eruptions on Europa using topography obtained from Galileo images. *Icarus* 361, 114373. doi:10.1016/j.icarus.2021.114373.
- Lowell, R.P., DuBose, M., 2005. Hydrothermal systems on Europa. *Geophysical Research Letters* 32. doi:10.1029/2005gl022375.
- Lumay, G., Boschini, F., Traina, K., Bontempi, S., Remy, J.C., Cloots, R., Vandewalle, N., 2012. Measuring the flowing properties of powders and grains. *Powder Technology* 224, 19–27. doi:10.1016/j.powtec.2012.02.015.
- Mandal, S., Nicolas, M., Pouliquen, O., 2020. Insights into the rheology of cohesive granular media. *Proceedings of the National Academy of Sciences* 117, 8366–8373. doi:10.1073/pnas.1921778117.
- Martin, E.S., Whitten, J.L., Kattenhorn, S.A., Collins, G.C., Southworth, B.S., Wiser, L.S., Prindle, S., 2023. Measurements of regolith thicknesses on Enceladus: Uncovering the record of plume activity. *Icarus* 392, 115369. URL: <https://www.sciencedirect.com/science/article/pii/S0019103522004614>, doi:<https://doi.org/10.1016/j.icarus.2022.115369>.
- Martin, W., Baross, J., Kelley, D., Russell, M.J., 2008. Hydrothermal vents and the origin of life. *Nature Reviews Microbiology* 6, 805–814. doi:10.1038/nrmicro1991.
- Mellmann, J., 2001. The transverse motion of solids in rotating cylinders - forms of motion and transition behavior. *Powder Technology* 118, 251–270.
- Mills, M.M., Pappalardo, R.T., Panning, M.P., Leonard, E.J., Howell, S.M., 2023. Moonquake-triggered mass wasting processes on icy satellites. *Icarus* , 115534URL: <https://www.sciencedirect.com/science/article/pii/S0019103523001112>, doi:<https://doi.org/10.1016/j.icarus.2023.115534>.
- Miyamoto, H., Mitri, G., Showman, A.P., Dohm, J.M., 2005. Putative ice flows on Europa: Geometric patterns and relation to topography collectively constrain material properties and effusion rates. *Icarus* 177, 413–424. doi:10.1016/j.icarus.2005.03.014.
- Musioli, G., Wurm, G., 2019. Contacts of Water Ice in Protoplanetary Disks - Laboratory Experiments. *The Astrophysical Journal* 873, 58. doi:10.3847/1538-4357/ab0428.
- Nakajima, M., Ingersoll, A.P., 2016. Controlled boiling on Enceladus. 1. Model of the vapor-driven jets. *Icarus* 272, 309–318. doi:10.1016/j.icarus.2016.02.027.
- Nedderman, R.M., 1992. *Statics and Kinematics of Granular Materials*. Cambridge University Press. doi:10.1017/CB09780511600043.
- Neveu, A., Francqui, F., Lumay, G., 2022. Measuring powder flow properties in a rotating drum. *Measurement* 200, 111548. doi:10.1016/j.measurement.2022.111548.
- Nimmo, F., Pappalardo, R.T., 2016. Ocean worlds in the outer solar system. *Journal of Geophysical Research: Planets* 121, 1378–1399. doi:10.1002/2016je005081.
- O'Rourke, L., Heinisch, P., Blum, J., Fornasier, S., Filacchione, G., Van Hoang, H., Ciarniello, M., Raponi, A., Gundlach, B., Blasco, R.A., Grieger, B., Glassmeier, K.H., Küppers, M., Rotundi, A., Groussin, O., Bockelée-Morvan, D., Auster, H.U., Oklay, N., Paar, G., del Pilar Caballo Perucha, M., Kovacs, G., Jorda, L., Vincent, J.B., Capaccioni, F., Biver, N., Parker, J.W., Tubiana, C., Sierks, H., 2020. The Philae lander reveals low-strength primitive ice inside cometary boulders. *Nature* 586, 697–701. doi:10.1038/s41586-020-2834-3.
- Pachón-Morales, J., Colin, J., Casalinho, J., Perré, P., Puel, F., 2020. Flowability characterization of torrefied biomass powders: Static and dynamic testing. *Biomass and Bioenergy* 138, 105608. doi:10.1016/j.biombioe.2020.105608.
- Poch, O., Cerubini, R., Pommerol, A., Jost, B., Thomas, N., 2018. Polarimetry of Water Ice Particles Providing Insights on Grain Size and Degree of Sintering on Icy Planetary Surfaces. *Journal of Geophysical Research : Planets* 123, 2564–2584. doi:10.1029/2018je005753.
- Poch, O., Pommerol, A., Jost, B., Carrasco, N., Szopa, C., Thomas, N., 2016. Sublimation of water ice mixed with silicates and tholins: Evolution of surface texture and reflectance spectra, with implications for comets. *Icarus* 267, 154–173. doi:10.1016/j.icarus.2015.12.017.
- Porco, C., DiNino, D., Nimmo, F., 2014. HOW THE GEYSERS, TIDAL STRESSES, AND THERMAL EMISSION ACROSS THE SOUTH POLAR TERRAIN OF ENCELADUS ARE RELATED. *The Astronomical Journal* 148, 45. doi:10.1088/0004-6256/148/3/45.
- Porco, C.C., Helfenstein, P., Thomas, P.C., Ingersoll, A.P., Wisdom, J., West, R., Neukum, G., Denk, T., Wagner, R., Roatsch, T., Kieffer, S., Turtle, E., McEwen, A., Johnson, T.V., Rathbun, J., Veverka, J., Wilson, D., Perry, J., Spitale, J., Brahic, A., Burns,

- J.A., DelGenio, A.D., Dones, L., Murray, C.D., Squyres, S., 2006. Cassini Observes the Active South Pole of Enceladus. *Science* 311, 1393–1401. URL: <https://www.science.org/doi/abs/10.1126/science.1123013>, doi:10.1126/science.1123013, arXiv:<https://www.science.org/doi/pdf/10.1126/science.1123013>.
- Postberg, F., Clark, R.N., Hansen, C.J., Coates, A.J., Dalle Ore, C.M., Scipioni, F., Hedman, M.M., Waite, J.H., 2018a. Plume and Surface Composition of Enceladus, in: Schenk, P.M., Clark, R.N., Howett, C.J.A., Verbiscer, A.J., Waite, J.H. (Eds.), *Enceladus and the Icy Moons of Saturn*. University of Arizona Press, p. 129. doi:10.2458/azu\$_uapress\$_9780816537075-ch007.
- Postberg, F., Khawaja, N., Abel, B., Choblet, G., Glein, C.R., Gudipati, M.S., Henderson, B.L., Hsu, H.W., Kempf, S., Klenner, F., Moragas-Klostermeyer, G., Magee, B., Nölle, L., Perry, M., Reviol, R., Schmidt, J., Srama, R., Stolz, F., Tobie, G., Trielloff, M., Waite, J.H., 2018b. Macromolecular organic compounds from the depths of Enceladus. *Nature* 558, 564–568. doi:10.1038/s41586-018-0246-4.
- Postberg, F., Schmidt, J., Hillier, J., Kempf, S., Srama, R., 2011. A salt-water reservoir as the source of a compositionally stratified plume on Enceladus. *Nature* 474, 620–622. doi:10.1038/nature10175.
- Prockter, L.M., Patterson, G.W., 2009. Morphology and evolution of Europa's ridges and bands, in: *Europa*. University of Arizona Press Tucson, pp. 237–258.
- Quick, L.C., Hedman, M.M., 2020. Characterizing deposits emplaced by cryovolcanic plumes on Europa. *Icarus* 343, 113667. doi:10.1016/j.icarus.2020.113667.
- Richefeu, V., El Youssoufi, M.S., Radjaï, F., 2006. Shear strength properties of wet granular materials. *Phys. Rev. E* 73, 051304. URL: <https://link.aps.org/doi/10.1103/PhysRevE.73.051304>, doi:10.1103/PhysRevE.73.051304.
- Robidel, R., Le Mouélic, S., Tobie, G., Massé, M., Seignovert, B., Sotin, C., Rodriguez, S., 2020. Photometrically-corrected global infrared mosaics of Enceladus: New implications for its spectral diversity and geological activity. *Icarus* 349, 113848. doi:10.1016/j.icarus.2020.113848.
- Rosenberg, R., 2005. Why Is Ice Slippery? *Physics Today* 58, 50–54. doi:10.1063/1.2169444.
- Roth, L., Saur, J., Retherford, K.D., Strobel, D.F., Feldman, P.D., McGrath, M.A., Nimmo, F., 2014. Transient Water Vapor at Europa's South Pole. *Science* 343, 171–174. doi:10.1126/science.1247051.
- Schenk, P., Hamilton, D.P., Johnson, R.E., McKinnon, W.B., Paranicas, C., Schmidt, J., Showalter, M.R., 2011. Plasma, plumes and rings: Saturn system dynamics as recorded in global color patterns on its midsize icy satellites. *Icarus* 211, 740–757. doi:10.1016/j.icarus.2010.08.016.
- Schmidt, B.E., Blankenship, D.D., Patterson, G.W., Schenk, P.M., 2011. Active formation of 'chaos terrain' over shallow subsurface water on Europa. *Nature* 479, 502–505. doi:10.1038/nature10608.
- Schmidt, J., Brilliantov, N., Spahn, F., Kempf, S., 2008. Slow dust in Enceladus' plume from condensation and wall collisions in tiger stripe fractures. *Nature* 451, 685–688. doi:10.1038/nature06491.
- Schubert, G., Anderson, J.D., Travis, B.J., Palguta, J., 2007. Enceladus: Present internal structure and differentiation by early and long-term radiogenic heating. *Icarus* 188, 345–355. doi:10.1016/j.icarus.2006.12.012.
- Schubert, G., Sohl, F., Hussmann, H., 2009. Interior of Europa. *Europa*, 353–367.
- Shock, E.L., 2007. Hydrothermal Systems as Environments for the Emergence of Life, in: *Novartis Foundation Symposia*. John Wiley & Sons, Ltd., pp. 40–60. doi:10.1002/9780470514986.ch3.
- Sotin, C., Tobie, G., 2004. Internal structure and dynamics of the large icy satellites. *Comptes Rendus Physique* 5, 769–780. doi:10.1016/j.crhy.2004.08.001.
- Southworth, B.S., Kempf, S., Schmidt, J., 2015. Modeling Europa's dust plumes. *Geophysical Research Letters* 42. doi:10.1002/2015gl066502.
- Southworth, B.S., Kempf, S., Spitale, J., 2019. Surface deposition of the Enceladus plume and the zenith angle of emissions. *Icarus* 319, 33–42. doi:10.1016/j.icarus.2018.08.024.
- Spahn, F., Schmidt, J., Albers, N., Hörning, M., Makuch, M., SeiB, M., Kempf, S., Srama, R., Dikarev, V., Helfert, S., Moragas-Klostermeyer, G., Krivov, A.V., Sremčević, M., Tuzzolino, A.J., Economou, T., Grün, E., 2006. Cassini Dust Measurements at Enceladus and Implications for the Origin of the E Ring. *Science* 311, 1416–1418. doi:10.1126/science.1121375.
- Sparks, W.B., Hand, K.P., McGrath, M.A., Bergeron, E., Cracraft, M., Deustua, S.E., 2016. PROBING FOR EVIDENCE OF PLUMES ON EUROPA WITH *HST/STIS*. *The Astrophysical Journal* 829, 121. doi:10.3847/0004-637x/829/2/121.
- Sparks, W.B., Schmidt, B.E., McGrath, M.A., Hand, K.P., Spencer, J.R., Cracraft, M., Deustua, S.E., 2017. Active Cryovolcanism on Europa? *The Astrophysical Journal* 839, L18. doi:10.3847/2041-8213/aa67f8.
- Spencer, J., Nimmo, F., Ingersoll, A.P., Hurford, T.A., Kite, E.S., Rhoden, A.R., Schmidt, J., Howett, C.J.A., 2018. Plume Origins and Plumbing (Ocean to Surface), in: *Enceladus and the Icy Moons of Saturn*. The University of Arizona Press, pp. 163–174. doi:10.2458/azu\$_uapress\$_9780816537075-ch008.
- Spencer, J.R., Nimmo, F., 2013. Enceladus: An Active Ice World in the Saturn System. *Annual Review of Earth and Planetary Sciences* 41, 693–717. URL: <https://doi.org/10.1146/annurev-earth-050212-124025>, doi:10.1146/annurev-earth-050212-124025, arXiv:<https://doi.org/10.1146/annurev-earth-050212-124025>.
- Spencer, J.R., Pearl, J.C., Segura, M., Flasar, F.M., Mamoutkine, A., Romani, P., Buratti, B.J., Hendrix, A.R., Spilker, L.J., Lopes, R.M.C., 2006. Cassini Encounters Enceladus: Background and the Discovery of a South Polar Hot Spot. *Science* 311, 1401–1405. URL: <https://www.science.org/doi/abs/10.1126/science.1121661>, doi:10.1126/science.1121661, arXiv:<https://www.science.org/doi/pdf/10.1126/science.1121661>.
- Spencer, J.R., Tamppari, L.K., Martin, T.Z., Travis, L.D., 1999. Temperatures on Europa from Galileo Photopolarimeter-Radiometer: Nighttime Thermal Anomalies. *Science* 284, 1514–1516. URL: <https://www.science.org/doi/abs/10.1126/science.284.5419.1514>, doi:10.1126/science.284.5419.1514, arXiv:<https://www.science.org/doi/pdf/10.1126/science.284.5419.1514>.
- Spitale, J.N., Hurford, T.A., Rhoden, A.R., Berkson, E.E., Platts, S.S., 2015. Curtain eruptions from Enceladus' south-polar terrain. *Nature* 521, 57–60. doi:10.1038/nature14368.
- Spitale, J.N., Porco, C.C., 2007. Association of the jets of Enceladus with the warmest regions on its south-polar fractures. *Nature* 449, 695–697. doi:10.1038/nature06217.

- Srama, R., Ahrens, T.J., Altobelli, N., Auer, S., Bradley, J.G., Burton, M., Dikarev, V.V., Economou, T., Fechtig, H., Görlich, M., Grande, M., Graps, A., Grün, E., Havnes, O., Helfert, S., Horanyi, M., Igenbergs, E., Jessberger, E.K., Johnson, T.V., Kempf, S., Krivov, A.V., Krüger, H., Mocker-Ahlreep, A., Moragas-Klostermeyer, G., Lamy, P., Landgraf, M., Linkert, D., Linkert, G., Lura, F., McDonnell, J.A.M., Möhlmann, D., Morfill, G.E., Müller, M., Roy, M., Schäfer, G., Schlotzhauer, G., Schwehm, G.H., Spahn, F., Stübig, M., Svestka, J., Tschernjawski, V., Tuzzolino, A.J., Wäsch, R., Zook, H.A., 2004. The Cassini Cosmic Dust Analyzer. *Space Science Reviews* 114, 465–518. doi:10.1007/s11214-004-1435-z.
- Stephan, K., Ciarniello, M., Poch, O., Schmitt, B., Haack, D., Raponi, A., 2021. VIS-NIR/SWIR Spectral Properties of H₂O Ice Depending on Particle Size and Surface Temperature. *Minerals* 11, 1328. doi:10.3390/min11121328.
- Taffin, C., Grasset, O., Le Menn, E., Bollengier, O., Giraud, M., Le Mouélic, S., 2012. Temperature and grain size dependence of near-IR spectral signature of crystalline water ice: From lab experiments to Enceladus' south pole. *Planetary and Space Science* 61, 124–134. doi:10.1016/j.pss.2011.08.015.
- Vance, S., Harnmeijer, J., Kimura, J., Hussmann, H., deMartin, B., Brown, J.M., 2007. Hydrothermal Systems in Small Ocean Planets. *Astrobiology* 7, 987–1005. doi:10.1089/ast.2007.0075.
- Waite, J.H., Combi, M.R., Ip, W.H., Cravens, T.E., McNutt, R.L., Kasprzak, W., Yelle, R., Luhmann, J., Niemann, H., Gell, D., Magee, B., Fletcher, G., Lunine, J., Tseng, W.L., 2006. Cassini Ion and Neutral Mass Spectrometer: Enceladus Plume Composition and Structure. *Science* 311, 1419–1422. URL: <https://www.science.org/doi/abs/10.1126/science.1121290>, doi:10.1126/science.1121290, arXiv:<https://www.science.org/doi/pdf/10.1126/science.1121290>.
- Yoldi, Z., Pommerol, A., Jost, B., Poch, O., Gouman, J., Thomas, N., 2015. VIS-NIR reflectance of water ice/regolith analogue mixtures and implications for the detectability of ice mixed within planetary regoliths. *Geophysical Research Letters* 42, 6205–6212.
- Zahnle, K., Schenk, P., Levison, H., Dones, L., 2003. Cratering rates in the outer Solar System. *Icarus* 163, 263–289. doi:10.1016/s0019-1035(03)00048-4.

Appendix

A. Derivation of the simple avalanche model

In the following, we derive a simple avalanche model based on the geometry sketched in Fig. A.1. The purpose of the model is to determine a scaling useful to estimate the surface energy of our materials as a function of the experimental measurements. In order to obtain a treatable scaling, some simplifying assumptions are employed, trying however to keep the main mechanical features of the problem.

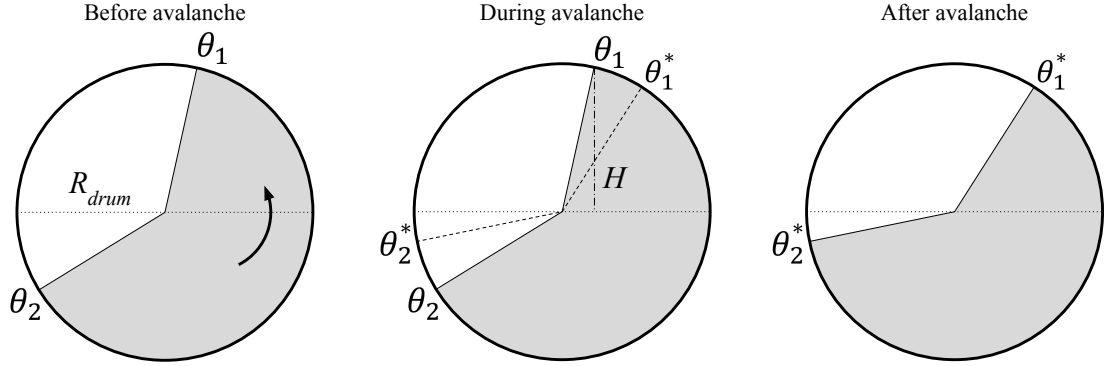


Figure A.1: Simplified model of an avalanche occurring inside the rotating drum device, inspired by classical theories on slopes stability.

We observed in the experiments that the powder surface is characterised by a double slope (defined by two angles θ_1 and θ_2). The upper slope (θ_1) destabilises once a critical angle is reached, and the failure appears approximately on a plane characterised by a lower angle (θ_1^*). The avalanche therefore creates a top slope angle θ_1^* and a bottom slope angle θ_2^* (where $\theta_1 - \theta_1^* \approx \theta_2 - \theta_2^*$ from mass conservation). This phenomenology suggests to analyse the problem with classical soil mechanics tools for slope stability. Due to the planar nature of the failure surface, we may employ some classical results from the literature, to link the failure angle to the slope angle (Nedderman, 1992):

$$\theta_1^* = \frac{\theta_1 + \delta}{2}, \quad (6)$$

where δ is the angle of internal friction. Another result from the method is the relation between the cohesive yield stress τ_c and the maximum upper slope angle:

$$\frac{\tau_c}{\rho g H} = \frac{1 - \cos(\theta_1 - \delta)}{4 \cos \delta \sin \theta_1}, \quad (7)$$

where ρ is the apparent density, g gravity, and H the characteristic height of the upper slope (which can be approximated by $H \approx R_{drum} \sin \theta_1$ which is the value for a half filled drum). Theoretical predictions exist, which give the cohesive threshold τ_c , as a function of particle scale and macroscopic parameters (Richefeu, El Youssoufi and Radjaï, 2006):

$$\tau_c = \frac{3\mu\phi Z F_c}{2\pi d^2}, \quad (8)$$

where ϕ is the solid fraction of the material, Z is the coordination number (the average number of contacts per grain), $\mu = \tan \delta$ the internal friction coefficient, F_c is the cohesive force. Several models exist for the latter, often involving the surface energy γ . The limit pull-off force for the JKR model (Johnson, Kendall and Roberts, 1971), for example, gives, for particles of equal diameter d :

$$F_c = \frac{3}{8} \pi \gamma d, \quad (9)$$

which leads to the following equation:

$$\tau_c = \frac{9}{16} \mu \phi Z \frac{\gamma}{d}. \quad (10)$$

Note that different adhesive models yield the same scaling for the pull-off force as Eq. 9, albeit with a different pre-factor (1/2 for the DMT model which is valid for small rigid spheres). We can see with Eq. 10 that the cohesive stress τ_c increases when the grain size is decreasing. We can then combine Eq. 7 and Eq. 10 to obtain the following equation for γ :

$$\gamma = \frac{4}{9} \frac{\rho_p g d R_{drum}}{Z \sin \delta} [1 - \cos(\theta_1 - \delta)], \quad (11)$$

where $\rho_p = \rho/\phi$ is the intrinsic density. This scaling may therefore provide an estimate for the surface energy as a function of the maximum slope angle and some material properties. In our experiments, based on previous literature, we used two robust indicators of the flowability of the powder in the drum, i.e. $\bar{\theta}$, the mean angle of the flowing surface, and σ_θ , the standard deviation around this angle. For cohesive powders, between successive avalanches the material in the drum performs a solid body rotation, the angles inside a drum for a cohesive material should follow a nearly uniform distribution. The standard deviation for such a distribution can be defined as:

$$\sigma_\theta = \sqrt{\frac{(\theta_{max} - \theta_{min})^2}{12}}, \quad (12)$$

where $\theta_{max} = \frac{\theta_1 + \theta_2}{2}$ and $\theta_{min} = \frac{\theta_1^* + \theta_2^*}{2}$ are respectively the maximum and minimum average slope angles. If we define $\Delta\theta = \theta_{max} - \theta_{min}$, it is easy to see that $\theta_1 - \theta_1^* = \Delta\theta$, which yields, together with 6,

$$\theta_1 = 2\Delta\theta + \delta = 4\sqrt{3}\sigma_\theta + \delta. \quad (13)$$

Entering this result into Eq. 11, we can see that the surface energy may be estimated through the following formula which involves only the standard deviation of the average angle :

$$\gamma = \frac{4}{9} \frac{\rho_p g d R_{drum}}{Z \sin \delta} [1 - \cos(4\sqrt{3}\sigma_\theta)]. \quad (14)$$

This formula requires knowledge of the coordination number Z and the internal angle of friction δ . Luckily, differently from τ_c , the internal angle of friction δ does not vary a lot from one material to another, and is usually found around 30° . First shear cell test measurements done on ice powders seem to actually give a value of $\delta_{ice} \approx 30^\circ$. The coordination number is comprised between 3 and 6, so an average value of 5 is acceptable.

Cohesive properties of ice powders analogous to fresh plume deposits on Enceladus and Europa

Supplementary material: Rotating drum device description

In the following, we present a complete description of the rotating drum system, in the interest of reproducibility. All the elements of the montage will be named and described in detail in the following appendix.

1 Rotating drum body

A 3D-sketch of the drum system is available in Fig. 1, to better understand the following description. The rotating drum consists in a solid brass cylinder, the inside of which is empty, and the volume containing the sample has a diameter of 64 mm for a width of 16.4 mm. The drum is made of two separate parts, a massive body that carries the sample, and the lid, also made of brass, that simply closes the device. It is important to keep the same material for the body and the lid, to avoid differential thermal contraction due to materials of different nature. Furthermore, thermally conductive material has to be preferred to build this device. The drum is designed to be lighted from the back to perform “shadowgraphy” analyses on the powder inside the drum so, in order to have a uniform light source, we used a diffusive back window. The front window of the drum is fully transparent, and both windows are made of polycarbonate.

We designed the drum device to be able to perform measurements at very low temperature, close to liquid nitrogen temperature, around 77 K at minimum. To this end, we avoided the use of glue or adhesive, by mounting the windows with screws. The back window is mounted on the body, while the front window is mounted on the lid. The lid itself is mounted on the body by the use of a “quarter-turn” system, visible in Fig. 1. This part has four grooves that can host screws attached to the body of the drum. The grooves have shoulders at the bottom, and a small rotation of the lid prevent it from coming off the body, thanks to these shoulders. Tightening the screws locks the lid in place, and prevents it from turning or moving.

We also chose the material of the windows in agreement with literature concerning adhesion of ice on several materials. Indeed, Makkonen [2012] showed that ice and glass may display a very strong adhesion between each other, which could alter the flow of ice powder inside the drum by strong interactions with the windows. To solve this issue, we chose to use polycarbonate windows that seem to be less adhesive [Murase and Nanishi, 1985].

2 Temperature control

The rotating drum experiment presented in this work is designed to perform measurements at very cold temperatures, close to the temperature of liquid nitrogen (around 77 K). To achieve such temperatures, we developed a cooling solution specifically designed for the drum size. It consists in a thin copper cylinder, with a diameter slightly bigger than the drum external diameter, that is placed around the drum to make a

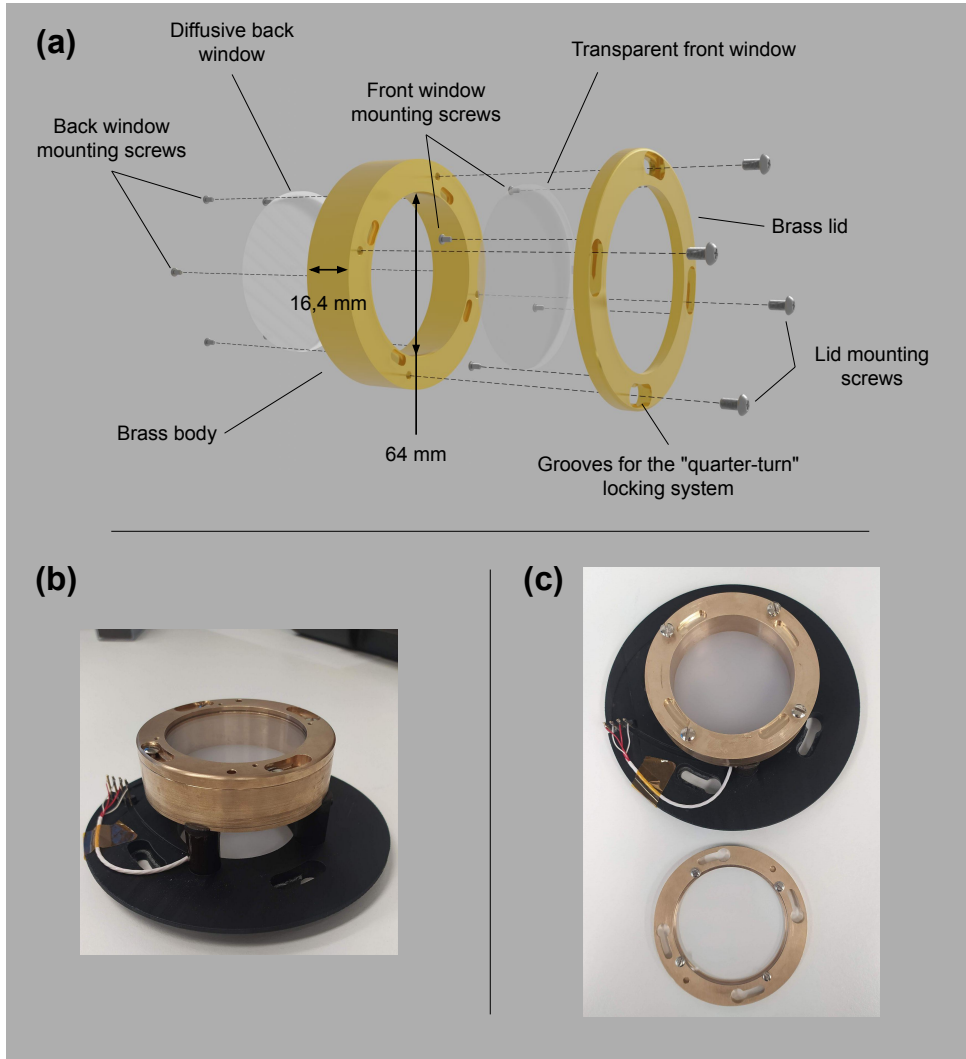


Figure 1: Illustration of the drum used in the experiments presented in the related paper. (a) Exploded 3D-view of the drum, with all the components. (b) Picture of the real drum device mounted on its stand, with the lid closed. (c) Picture of the real drum device, with the lid opened.

slight contact between these two elements. This copper cylinder has grooves on its external face, that carry a copper pipe coiled several times around the cylinder in order to maximise thermal exchanges (Fig. 2a). This pipe is connected to a liquid nitrogen tank on one side, and to a vacuum pump on the other side, thanks to flexible joints. The pump, while in operation, allows the liquid nitrogen to flow through the copper pipe, and to cool down this element and the drum, by conduction. The nitrogen flow rate can be regulated by a needle valve.

The copper cylinder is stationary, mounted on a stand, while the drum is rotating, and the small difference of diameter allows a slight contact even when the drum is in motion, so that the copper part is still cooling the system during acquisitions. In opposition to the cooling effect of the liquid nitrogen, we installed on the cooling copper part two heating resistors, glued by a refractory cement. These resistors are identical, placed at two opposite points on the copper cylinder, and they are two 20 W FIREROD

cartridge heater from the Watlow company. They can be controlled by the electrical current they receive, and when they are combined with the needle valve to regulate the nitrogen flow, it is possible to achieve steady temperature levels inside the drum.

To accurately measure the temperature of all the elements of the system, we used several temperature sensors placed on various locations. A first sensor, a thermocouple, is placed on the copper cooling part to control the power of the heating resistors and the flow rate of nitrogen. For more precise measurements and acquisitions, a Pt100 probe is placed directly in the brass body of the drum, close to the sample. As the drum, and so the probe, are rotating during the acquisitions, we developed a system of stationary and circular conductive tracks, coupled with rotating contact sensors, linked to the Pt100 probe and with their tips in contact with the tracks. As the drum and its stand are rotating, the contact sensors also rotate, but the electrical current from the probe is maintained thanks to the contact with the circular tracks, allowing us to read the temperature inside the drum even during an acquisition (Fig. 2b).

3 External systems

To cover the whole range of flowing behaviours inside the drum described by Mellmann [2001], it is necessary to cover the range of Froude numbers going from $Fr = 10^{-5}$ to $Fr \geq 1$. As a reminder, the Froude number Fr is the ratio between centrifugal force and gravity force,

$$Fr = \frac{\omega^2 R}{g}, \quad (1)$$

where ω represents the rotation speed of the drum, in rad.s^{-1} , R is the radius of the drum in m, g is the gravity, in m.s^{-2} .

The previous values of Froude number, considering a drum diameter of 64 mm, correspond to rotation speeds ω ranging from $\omega = 0.53$ RPM to $\omega \geq 167.20$ RPM. To perform such rotation speeds, we used the rotation motor Zaber X-RSB120AD, a programmable rotating plate that can achieve rotation speeds up to $\omega = 500$ RPM, and visible on the 3D sketch in Fig. 2a. This motor all has a hole in the centre, that allows the light to go through it, to illuminate the back of the drum. The drum is mounted to the motor by using a stand with columns that are 2.3 cm high, and the stand is maintained on the motor by the same “quarter-turn” system used to close the lid of the drum. The rotating plate is placed vertically, to put the drum in a horizontal condition. To make sure that this device is operating in good environmental conditions, and to avoid damage from cold temperature conditions, we protected it with a carter, and this enclosure is heated thanks to an auto-regulated resistor, with a power of 60 W (DBK-enclosures).

To ensure a good quality analysis of the powder flow inside the drum, we used a high resolution (2440×2048 pixels) colour camera, the camera Basler acA2440-75uc, that can acquire images up to 75 images per second. This acquisition device can be plugged on a computer, and controlled by a proprietary software, Pylon, but also by a Python library. Thus, we are able to control both the rotating motor and the camera with the same Python script, to synchronise the rotations of the drum and the image acquisitions, in a completely automated process. The camera is also equipped with a

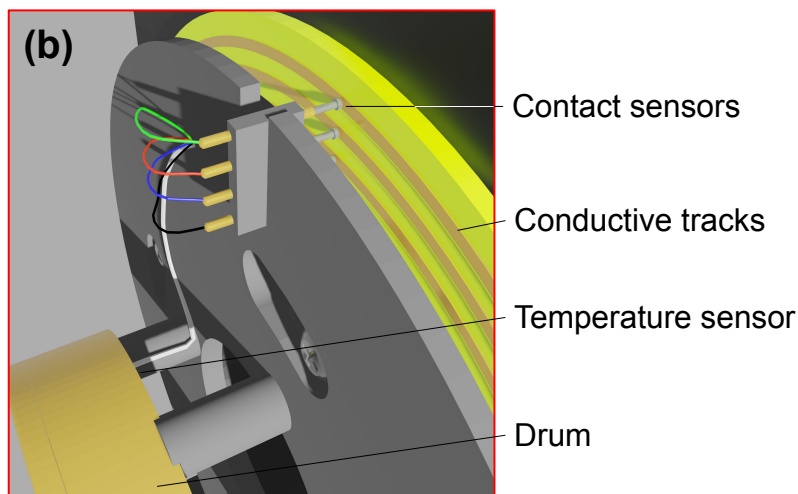
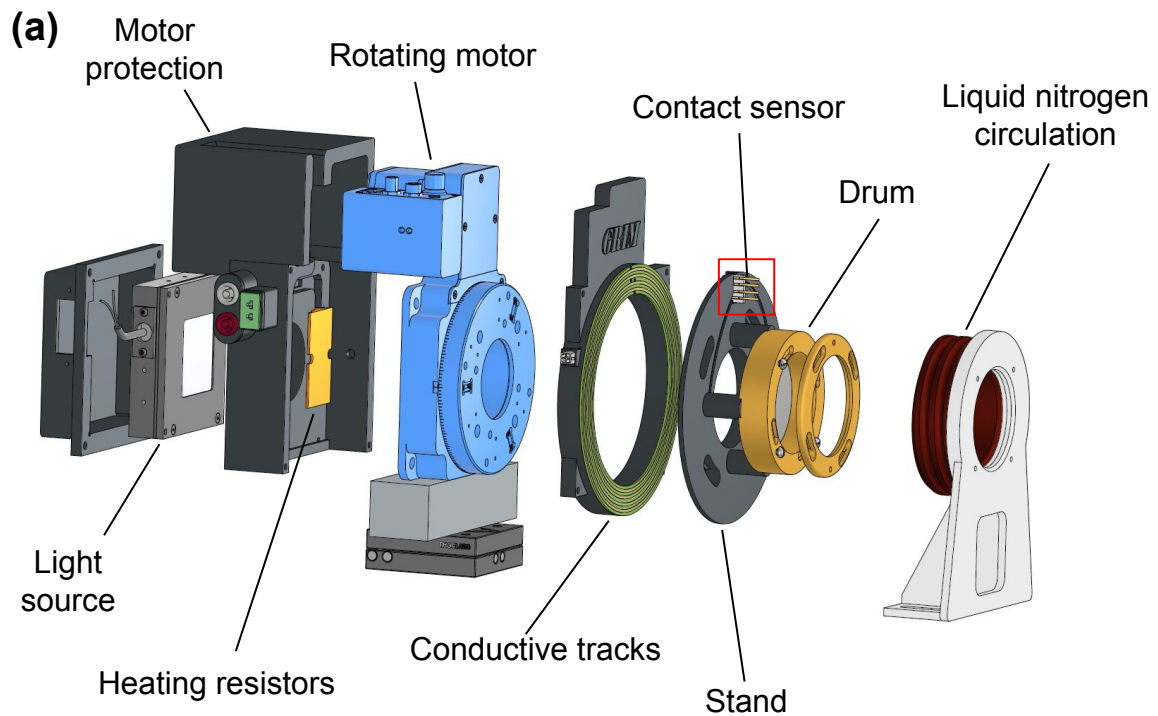


Figure 2: 3D illustrations of all the elements constituting the drum device. (a) Exploded view showing all the elements disassembled. (b) Detail of the contact sensors on the conductive tracks.

50 mm lens to reduce perspective and deformation effects of the camera itself, and to maximise the light captured by the image sensor. This device, as it is very sensitive to temperature, is also placed in a heated carter, together with a resistor similar to the one heating the rotating motor, and with a power of 20 W. The camera is placed in front of the drum, at a large enough distance to ensure that the whole surface of the drum is captured.

As mentioned in Sec. 1, we illuminate the drum from behind, by using a col-

limited light source, meaning that all the light rays emerging from this source are parallel. The model used for developing this rotating drum device is the MB-CBL2x2-W-24Z, a 2×2 inches LED panel from the Metaphase Lighting Technologies company. This light source is located behind the rotating motor, illuminating the device through the hole, and the panel is enclosed in the same carter as the motor, heated with the same resistor (Fig. 2a).

To prevent as much as possible the contamination of our samples by atmospheric moisture, we place the whole rotating drum device, consisting of the light source, the motor, the drum and the camera, in a dried cold chamber at 248 K, inside a custom built insulating box. We also put in this box silica-gel beads to absorb any residual moisture in the cold air of the chamber.

To monitor the temperature of all the systems, the light with the motor, the camera, but also the drum itself, we are using a external monitoring system, an acquisition unit from the AOIP company, the FRONTDAQ 5 or FD5. This unit is connected to a central computer that controls the motor, the camera, and also shows the temperature measurement of each sensitive device. The heating of the drum is performed by using a control unit, the MercuryiTC from the Oxford Instruments company that can regulate the power of the heating resistors. The computer, acquisition unit and control unit are placed outside the cold chamber to prevent any damage from condensation or cold temperatures, and they are connected to the experiment itself by cables running through the walls of the chamber.

References

- Makkonen, L., 2012. Ice Adhesion - Theory, Measurements and Countermeasures. *Journal of Adhesion Science and Technology* 26, 413–445. doi:10.1163/016942411x574583.
- Mellmann, J., 2001. The transverse motion of solids in rotating cylinders - forms of motion and transition behavior. *Powder Technology* 118, 251–270.
- Murase, H., Nanishi, K., 1985. On the Relationship of Thermodynamic and Physical Properties of Polymers With Ice Adhesion. *Annals of Glaciology* 6, 146–149. doi:10.3189/1985aog6-1-146-149.